



# Selective Serotonin Reuptake Inhibitors within Cells: Temporal Resolution in Cytoplasm, Endoplasmic Reticulum, and Membrane

 Aaron L. Nichols,<sup>1\*</sup> Zack Blumenfeld,<sup>1,2\*</sup> Laura Luebbert,<sup>1,3</sup> Hailey J. Knox,<sup>4</sup> Anand K. Muthusamy,<sup>4</sup> Jonathan S. Marvin,<sup>5</sup> Charlene H. Kim,<sup>1</sup> Stephen N. Grant,<sup>4</sup> David P. Walton,<sup>4</sup> Bruce N. Cohen,<sup>1</sup> Rebekkah Hammar,<sup>6</sup> Loren Looger,<sup>5</sup> Per Artursson,<sup>6,7</sup> Dennis A. Dougherty,<sup>4</sup> and  Henry A. Lester<sup>1</sup>

<sup>1</sup>Division of Biology and Biological Engineering, California Institute of Technology, Pasadena, California 91106, <sup>2</sup>Keck School of Medicine, University of Southern California, Los Angeles, California 90007, <sup>3</sup>Institute of Biology, Leiden University, 2333 BE Leiden, The Netherlands, <sup>4</sup>Division of Chemistry and Chemical Engineering, California Institute of Technology, Pasadena, California 91106, <sup>5</sup>Janelia Research Campus, Howard Hughes Medical Institute, Ashburn, Virginia 20147, <sup>6</sup>Department of Pharmacy, Uppsala University, SE-751 23 Uppsala, Sweden, and <sup>7</sup>Science for Life Laboratory Drug Discovery and Development Platform and Uppsala University Drug Optimization and Pharmaceutical Profiling Platform, Uppsala University, SE-751 23 Uppsala, Sweden

Selective serotonin reuptake inhibitors (SSRIs) are the most prescribed treatment for individuals experiencing major depressive disorder. The therapeutic mechanisms that take place before, during, or after SSRIs bind the serotonin transporter (SERT) are poorly understood, partially because no studies exist on the cellular and subcellular pharmacokinetic properties of SSRIs in living cells. We studied escitalopram and fluoxetine using new intensity-based, drug-sensing fluorescent reporters targeted to the plasma membrane, cytoplasm, or endoplasmic reticulum (ER) of cultured neurons and mammalian cell lines. We also used chemical detection of drug within cells and phospholipid membranes. The drugs attain equilibrium in neuronal cytoplasm and ER at approximately the same concentration as the externally applied solution, with time constants of a few s (escitalopram) or 200–300 s (fluoxetine). Simultaneously, the drugs accumulate within lipid membranes by  $\geq 18$ -fold (escitalopram) or 180-fold (fluoxetine), and possibly by much larger factors. Both drugs leave cytoplasm, lumen, and membranes just as quickly during washout. We synthesized membrane-impermeant quaternary amine derivatives of the two SSRIs. The quaternary derivatives are substantially excluded from membrane, cytoplasm, and ER for  $>2.4$  h. They inhibit SERT transport-associated currents sixfold or 11-fold less potently than the SSRIs (escitalopram or fluoxetine derivative, respectively), providing useful probes for distinguishing compartmentalized SSRI effects. Although our measurements are orders of magnitude faster than the therapeutic lag of SSRIs, these data suggest that SSRI–SERT interactions within organelles or membranes may play roles during either the therapeutic effects or the antidepressant discontinuation syndrome.

**Key words:** inside-out pharmacology; biosensor; escitalopram; fluoxetine; iDrugSnFRs; pharmacokinetics

Received July 29, 2022; revised Nov. 2, 2022; accepted Nov. 27, 2022.

Author contributions: A.L.N., Z.B., L. Luebbert, H.J.K., A.K.M., J.S.M., C.H.K., S.N.G., D.P.W., R.H., L. Looger, P.A., D.A.D., and H.A.L. designed research; A.L.N., Z.B., L. Luebbert, H.J.K., A.K.M., J.S.M., C.H.K., S.N.G., D.P.W., and R.H. performed research; A.L.N., Z.B., L. Luebbert, H.J.K., A.K.M., J.S.M., S.N.G., D.P.W., B.N.C., R.H., P.A., D.A.D., and H.A.L. analyzed data; A.L.N., Z.B., L. Looger, and H.A.L. wrote the paper.

A.L.N. was supported by California Tobacco-Related Disease Research Program (TRDRP) Grant 27FT-0022; H.A.L. was supported by California TRDRP Grant 27IP-0057, National Institutes of Health (NIH)–National Institute of General Medical Sciences (NIGMS) Grant GM-123582, NIH–National Institute on Drug Abuse grant NS105595, and NIH–National Institute of Mental Health Grant MH120823; D.A.D. was supported by California TRDRP Grant T29IR0455; A.K.M. was supported by NIH–National Institute on Drug Abuse Grant DA049140 and NIH–NIGMS Grant GM7616; J.S.M. and L. Looger were supported by the Howard Hughes Medical Institute; L. Luebbert was supported by Leiden University International Studies Fund Grant LISF L18020-1-45; P.A. was supported by Swedish Research Council Grant 01586; and R.H. was supported by the

European Union Horizon 2020 Research and Innovation Program under Marie Skłodowska-Curie Grant Agreement 956851. We thank Stefan Petrovic for stewardship of the isothermal titration calorimeter in the Caltech Center for Molecular Medicine; the Gradinaru lab and Caltech CLOVER Center for help with viral vectors; Andres Collazo and Giada Spigolon at the Caltech Biological Imaging Facility; Stefan Trapp for furnishing and explaining the original version of the Microsoft Excel workbook for acid trapping; Zoe Beatty, Kallol Bera, Eve Fine, Shan Huang, Elaine Lin, Stephen Mayo, Lin Tian, Andrea Treyer, Elizabeth Unger, and Lu Wei for advice and guidance; and Purnima Deshpande for lab management.

\*A.L.N. and Z.B. share co-first authorship.

The authors declare no competing financial interests.

Correspondence should be addressed to Henry A. Lester at lester@caltech.edu.

<https://doi.org/10.1523/JNEUROSCI.1519-22.2022>

Copyright © 2023 the authors

### Significance Statement

Selective serotonin reuptake inhibitors stabilize mood in several disorders. In general, these drugs bind to SERT, which clears serotonin from CNS and peripheral tissues. SERT ligands are effective and relatively safe; primary care practitioners often prescribe them. However, they have several side effects and require 2–6 weeks of continuous administration until they act effectively. How they work remains perplexing, contrasting with earlier assumptions that the therapeutic mechanism involves SERT inhibition followed by increased extracellular serotonin levels. This study establishes that two SERT ligands, fluoxetine and escitalopram, enter neurons within minutes, while simultaneously accumulating in many membranes. Such knowledge will motivate future research, hopefully revealing where and how SERT ligands engage their therapeutic target(s).

### Introduction

The approval of fluoxetine (Prozac), the first serotonin reuptake inhibitor (SSRI), in 1986 transformed treatment of major depressive disorder (MDD). Prescribed regimens for MDD still use fluoxetine and other SSRIs, such as escitalopram (Lexapro; Wong et al., 1974, 1995; Beasley et al., 2000; Baldwin, 2002; Burke et al., 2002; Lepola et al., 2003; Lalit et al., 2004; Wong et al., 2005; Rao, 2007; Kennedy et al., 2009).

However, fascinating neuroscientific questions remain about the mechanism(s) of SSRI therapy. Answering the question, Where do SSRIs go? is necessary, but admittedly not sufficient, to address uncertainties surrounding SSRI mechanisms and modes of action. Therefore, this article develops and exploits tools to study movements of fluoxetine and escitalopram within cells.

The experiments were conducted against the background of four nonmutually exclusive mechanisms that might explain SSRI action, presented in order of increasing novelty. First, the eponymous inhibition of the plasma membrane serotonin transporter (SERT) would increase extracellular serotonin levels, eventually causing (via unexplained intracellular mechanisms) amelioration of the clinical symptoms of MDD (Clevenger et al., 2018); we have termed this the “outside-in” mechanism (Lester et al., 2012). Although serotonin levels in the synaptic cleft are rapidly altered after SSRI administration, a therapeutic lag of 2–6 weeks indicates a more complex mode of action (Nierenberg et al., 2000; Belmaker and Agam, 2008; Malhi and Mann, 2018). Depletion of serotonin in healthy individuals does not produce depressive effects, also suggesting that increased extracellular serotonin may be only one component of SSRI action (Salomon et al., 1997).

Second, the therapeutic lag may result mostly from a 10 d (or longer) buildup of SSRI levels, eliminating the necessity for complex outside-in mechanisms but raising fundamental questions about SSRI pharmacokinetics. The steady-state CSF concentrations in patients during escitalopram and fluoxetine treatment are 17–115 nM (Paulzen et al., 2016) and  $13 \pm 6 \mu\text{M}$  (Karson et al., 1992; Renshaw et al., 1992; Bolo et al., 2000), respectively (although the CSF fluoxetine concentration is confounded by simultaneous detection of both fluoxetine and its metabolite norfluoxetine). The apparent volume of distribution values for escitalopram ( $20 \text{ L kg}^{-1}$ ; Søgaard et al., 2005) and fluoxetine ( $20\text{--}42 \text{ L kg}^{-1}$ ; Lee-Kelland et al., 2018) indicate substantial accumulation of each drug in tissues. Volume of distribution is sometimes correlated with increasingly positive  $\text{LogD}_{\text{pH}7.4}$  values; escitalopram (1.41) and fluoxetine (1.83) follow this trend.

Third, vaguely defined “inside-out” mechanisms postulate that SSRIs enter the organelles of the early exocytotic pathway,

where binding to nascent SERT may induce unconventional mechanisms such as pharmacological chaperoning (Lester et al., 2012). Thus, inside-out mechanisms would begin with SSRI–SERT binding, but in compartments distinct from the plasma membrane and via effects other than 5-HT reuptake. These mechanisms would cause the therapeutic lag.

Fourth, SSRIs may relieve MDD through additional mechanisms, involving targets other than SERT. Possible pathways include: activation of the brain-derived neurotrophic factor (BDNF) receptor tyrosine kinase reporter 2 (TRKB; Casarotto et al., 2021); and lipid rafts (Senese and Rasenick, 2021).

We used several methods. Analogous to recent work on the subcellular pharmacokinetics of other neuropsychiatric drugs (Bera et al., 2019; Shivange et al., 2019; Muthusamy et al., 2022; Nichols et al., 2022), we developed and applied new intensity-based, drug, sensing fluorescent reporters (iDrugSnFRs) for SSRIs, targeted to the plasma membrane (PM), cytoplasm, and endoplasmic reticulum (ER). We detected fluorescence increases resulting from  $\sim 1 \text{ s}$  solution changes near cultured neurons and HeLa cells. We chemically detected drug accumulation by cultured cells and phospholipid-coated beads. We also synthesized membrane-impermeant quaternary amine derivatives of escitalopram and fluoxetine and compared their movements and SERT pharmacology to those of the SSRIs.

The subcellular pharmacokinetic data are more complex than expected from biophysical and biochemical studies on the iDrugSnFRs in solution or from our previous work on other CNS-acting drugs. The data provide insight into three of the four potential mechanisms of SSRI action in the CNS.

### Materials and Methods

*Experimental design and statistical analysis.* All concentration–response experiments using purified iDrugSnFR protein were performed in triplicate. The SD was calculated for each data point acquired. Isothermal titration calorimetry (ITC) experiments were performed in triplicate, and the SEM was calculated. Half-maximal inhibitory concentration ( $\text{IC}_{50}$ ) measurements for escitalopram, fluoxetine, and their quaternary derivatives were from at least 10 cells, from which the SEM was calculated. Stopped-flow experiments were repeated five times and averaged, from which SDs were calculated (except for 100 s experiments, which were collected only once). Experiments utilizing mammalian cell culture and mouse primary hippocampal culture were designed in such a way that fluorescence response was averaged across at least five cells from at least two distinct fields of view, after which the SEM was calculated.

*Directed evolution of iDrugSnFR proteins using bacterial expression.* Starting with iAChSnFR and intermediate biosensor constructs of that sensor, we constructed and optimized biosensors for each drug partner during iterative rounds of site-saturated mutagenesis (SSM) as previously described (Bera et al., 2019; Borden et al., 2019; Shivange et al., 2019; Unger et al., 2020). We used the 22-codon procedure including a mixture of three primers, creating 22 unique codons encoding the 20

canonical amino acids (Kille et al., 2013). The 22-codon procedure yields an estimated >95% residue coverage for a collection of 96 randomly chosen clones.

A Spark M10 96-well fluorescence plate reader (Tecan) was used to measure resting and drug-induced fluorescence ( $F_0$  and  $\Delta F$ , respectively). Bacterial lysates were tested with excitation at 485 nm and emission at 535 nm. Lysates were also measured against choline to evaluate potential endogenous intracellular binding. Promising clones were amplified and sequenced. The optimally responding construct in each round of SSM was used as a template for the next round.

S-slope allows for comparison between iDrugSnFRs with differing  $\Delta F_{max}/F_0$  values (Bera et al., 2019) at the beginning of the concentration–response relation, which is typically the pharmacologically relevant range. With lysates or purified protein, which allow complete concentration–response relations, the Hill coefficient is near 1.0. We therefore calculated the following:

$$S\text{-slope} = \frac{\Delta F_{max}}{F_0} / EC_{50},$$

in units of  $\mu\text{M}^{-1}$ .

**Measurements on purified iDrugSnFRs.** Biosensors selected for further study were purified via the His<sub>6</sub> sequence using an ÄKTA Start FPLC (Fast Protein Liquid Chromatograph; GE Healthcare) as previously described (Shivange et al., 2019). Performance of protein quantification and concentration–response relations for drug-sensor partners was also as previously described (Shivange et al., 2019).

**ITC.** ITC experiments were performed on an Affinity ITC (TA Instruments) at 25°C. Biosensor protein was buffer exchanged into 3× PBS, pH 7.0. The SSRIs were dissolved in the same buffer, and 450  $\mu\text{M}$  escitalopram (Tocris Bioscience) was titrated into 45  $\mu\text{M}$  iEscSnFR, and 700  $\mu\text{M}$  *N,N*-dimethylfluoxetine was titrated into 140  $\mu\text{M}$  iFluoxSnFR. Analysis, including correction for changes in enthalpy generated from the dilution of the ligands into the cell during titration, was performed using a single-site binding model using NanoAnalyze software (TA Instruments).

**Stopped-flow kinetic analysis.** Kinetics were determined by mixing equal volumes of 0.2  $\mu\text{M}$  iDrugSnFR protein (in 3× PBS, pH 7.0) with varying concentrations of cognate ligand in an Applied Photophysics SX20 stopped-flow fluorimeter with 490 nm LED excitation and 510 nm long-pass filter at room temperature (22°C). Mixing shots were repeated five times and averaged (except for 100 s experiments, which were collected only once). SDs are not included on the plots but are nearly the same size as the data markers. The first 3 ms of data were ignored because of mixing artifacts and to account for the dead time of the instrument. Data were plotted and time courses were fitted, when possible, to a single exponential, with rate constant  $k_{obs}$ . When the time course did not fit well to a single rising exponential, it was fitted to the sum of two increasing exponentials.

**Synthesis of *N*-methylescitalopram and *N,N*-dimethylfluoxetine.** Synthesis of *N*-methylescitalopram was as previously published, with escitalopram replacing citalopram as the starting reagent (Bismuth-Evenzal et al., 2010). To generate *N,N*-dimethylfluoxetine, fluoxetine hydrochloride (60 mg, 0.174 mmol; Sigma-Aldrich) was dissolved in MeCN (5 ml). Et<sub>3</sub>N (130  $\mu\text{l}$ , 5 equiv) was added, followed by MeI (324  $\mu\text{l}$ , 30 equiv). The reaction was stirred at room temperature for 20 min. EtOAc (10 ml) was added, and the resulting precipitate was removed by filtration. The filtrate was concentrated, dissolved in dichloromethane, and washed with water (3×). The organic layer was dried over MgSO<sub>4</sub> and concentrated to give a yellow oil (44 mg, 54%). <sup>1</sup>H-NMR (400 MHz, CDCl<sub>3</sub>),  $\delta$  7.46–7.29 (m, 7H), 6.97 (d,  $J$  = 9.05 Hz, 2H), 5.57 (dd,  $J$  = 6.32 Hz 1H), 4.22–4.15 (m, 1H), 3.80–3.73 (m, 1H), 3.38 (s, 9H), 2.41–2.35 (m, 2H). ESI, M<sup>+</sup> calculated for C<sub>19</sub>H<sub>23</sub>F<sub>3</sub>NO<sup>+</sup> 338.17, found 338.22.

**Expression in HeLa cells.** We constructed three variants of each iDrugSnFR for expression in mammalian cells. The plasma membrane (suffix, \_PM) and endoplasmic reticulum (suffix, \_ER) variants were synthesized using circular polymerase extension cloning (Quan and Tian, 2009). To create the \_PM constructs, we cloned the bacterial constructs

into pCMV(MinDis), a variant of pDisplay (Thermo Fisher Scientific) lacking the hemagglutinin tag but including a transmembrane anchoring sequence (Marvin et al., 2013; Shivange et al., 2019; Nichols et al., 2022). To generate the \_ER constructs, we replaced the 14 C-terminal amino acids (QVDEQKLISEEDLN, including the Myc tag) with an ER retention motif, QTAEKDEL (Shivange et al., 2019). The \_ER constructs lack a transmembrane sequence and are designed to report on ligand concentration within the lumen of the ER. To generate the cytoplasm-targeted (suffix, \_cyto) variants, we used Gibson assembly (Gibson et al., 2009) to remove existing N- and C-terminal tags and incorporated an N-terminal strong nuclear exclusion sequence (NES; DIDELALKFAGLDL; Güttler et al., 2010).

We transfected the iDrugSnFR cDNA constructs into HeLa cells. Cell lines were purchased from ATCC and cultured according to ATCC protocols. For chemical transfection, we used either Lipofectamine 2000 or Lipofectamine 3000 (Thermo Fisher Scientific), following the recommended protocol of the manufacturer. Cells were incubated in the transfection medium for 24 h and imaged 24–48 h after transfection.

**AAV production and transduction in primary mouse hippocampal neuronal culture.** The adeno-associated virus (AAV) plasmid vector AAV9-hSyn was described previously (Challis et al., 2019). PM- and ER-targeted virus was purified using the AAVpro Purification Kit (Takara Bio). Cytoplasm-targeted virus was purified according to Challis et al., 2019. Mouse embryo dissection and culture were previously described (Shivange et al., 2019). Approximately 4 d after dissection, \_ER constructs were transduced at a multiplicity of infection (MOI) of 0.5–5 × 10<sup>4</sup>, \_PM constructs at an MOI of 0.5–1 × 10<sup>5</sup>, and \_cyto constructs at an MOI of 5 × 10<sup>4</sup>. Neurons were imaged ~2–3 weeks post-transduction.

**Time-resolved fluorescence measurements in live mammalian cells and primary mouse hippocampal neuronal culture.** Time-resolved concentration–response imaging was performed on a modified Olympus IX-81 microscope (wide-field epifluorescence mode using a 40× lens). Images were acquired at 2–4 frames/s with a back-illuminated Electron Microscopy CCD camera (iXon DU-897, Andor Technology) controlled by Andor IQ3 software. Fluorescence measurements at  $\lambda_{ex}$  = 470 nm  $\lambda_{em}$  = 535 nm used the previously described epifluorescence cube (Srinivasan et al., 2011; Shivange et al., 2019).

Solutions were delivered from elevated reservoirs by gravity flow, via solenoid valves (Automate Scientific), providing solution changes in the imaging chamber with a time constant < 10 s. The vehicle was HBSS. Other details have been described (Srinivasan et al., 2011; Shivange et al., 2019). Data analysis procedures included subtraction of blank (extracellular) areas and corrections for baseline drifts using OriginPro 2018 software.

For folimycin incubation experiments, primary hippocampal culture dishes were incubated with 80 nM folimycin (Sigma-Aldrich) for 10 min before the standard time-resolved concentration–response imaging outlined above (Tischbirek et al., 2012).

**Spinning disk confocal fluorescence images.** HeLa cells and mouse primary hippocampal culture were transfected or transduced as described above. Live-cell images were collected using a Nikon Ti-2E spinning disk laser scanning confocal inverted microscope through a 100× objective, 1.49 NA (oil), 120  $\mu\text{m}$  working distance. The laser wavelength was 488 nm at 15% power. Dishes were imaged in a custom incubator (Okolab) at 37°C and 5% CO<sub>2</sub>. Initial images were taken in HBSS. To add drug, we doubled the bath volume by adding HBSS containing drug, using a hand-held pipette. The final drug concentrations for each set of experiments were 10  $\mu\text{M}$  escitalopram and 10  $\mu\text{M}$  fluoxetine. Nikon Elements.nd2 output files were analyzed using FIJI. For Figures 3 and 7, we applied the same brightness/contrast settings to both members of each pair of pre- vs. post-drug panels for a particular construct (e.g., panels A1 and A2).

**Probing inhibition of hSERT activity using electrophysiology.** Human SERT (hSERT) cDNA was transferred to the pOTV vector (a gift from Mark Sonders, Columbia University). The K490T mutation (Cao et al., 1997) was made using the QuikChange protocol (Agilent). cDNA was linearized with NotI digestion (New England Biolabs) and purified using the QiaQuick PCR Purification kit (Qiagen). Purified DNA was then transcribed *in vitro* using the T7 mMessage mMachine kit (Ambion). *Xenopus laevis* oocytes were isolated, injected with cRNA (20 ng in 50 nl

nuclease-free water), and incubated at 19°C for 3 d in Ca<sup>2+</sup>-free ND96 solution containing the following (in mM): 96 NaCl, 2 KCl, 1 MgCl<sub>2</sub>, and 5 HEPES, pH 7.5, supplemented with 0.05 mg/ml gentamycin (Sigma-Aldrich), 2.5 mM sodium pyruvate (Acros Organics), and 0.67 mM theophylline (Sigma-Aldrich).

Two-electrode voltage-clamp electrophysiology was performed on an OpusXpress 6000A (Molecular Devices) at 20–25°C. All compound solutions were prepared using Ca<sup>2+</sup>-free ND96 solution, pH 5.5. Solution containing only SSRI or quaternary derivative (0.67 ml) was applied to oocytes over 10 s, followed by a 10 s incubation. Solution containing the same concentration of SSRI/quaternary derivative and 3 μM 5-HT (1 ml) was then applied over 15 s. This process was followed by a 3.2 min wash-out period at a buffer flow rate of 3 ml/min (see Fig. 10).

Oocytes were impaled with borosilicate glass electrodes filled with 3 M KCl (0.3–3.0 MΩ resistance) and held at –60 mV. Ca<sup>2+</sup>-free ND96 solution, pH 7.5, was used as a running buffer. Using Clampfit 10.3 software (Molecular Devices), we employed a low-pass Gaussian filter at 5 Hz, then subtracted the average baseline current preceding application of compound solutions in low-pH buffer. For each cell, peak currents at each concentration were normalized to the maximum transport-associated current (Mager et al., 1994) measured by applying 3 μM 5-HT in the absence of inhibitor (see Fig. 10). Normalized currents were then averaged and fitted to the Hill equation using Prism 9 (GraphPad).

**LogD calculations.** We used Chemalize (<https://chemaxon.com/products/chemicalize>) to calculate LogP and pK<sub>a</sub>. The software then calculates the following:

$$\text{LogD}_{\text{pH}7.4} = \text{LogP} - \log[1 + 10^{7.4 - \text{pK}_a}].$$

**Simulations of diffusion and binding.** The simulation approximates Fick's law as a sequence of fluxes between nested intracellular and extracellular shell compartments, governed by first-order rate constants  $k_f = k_b$  (Yu et al., 2016). Each shell is treated as a well-stirred compartment. The units and dimensions are those used by Yu et al. (2016), including μm, fL (μm<sup>3</sup>), ms, and molarity (fM, μM, or M). Most shells have a thickness of 0.495, 0.500, or 0.505 μm. For fluxes between shells, the effective diffusion constant is the free-solution value.

In classical analyses (Yu et al., 2016), the membrane barrier is not a shell; it is infinitely thin and has zero volume. In the model, the membrane barrier is located at a radius of 7.505 μm, and its permeability is represented by a single equal pair of rate constants,  $k_f = k_b$ , for flux between one pair of neighboring shells.

The permeability of the membrane barrier is calculated as though it were a shell of finite volume, with thickness 0.01 μm (10 nm), twice the value assumed by Kapoor et al. (2019) to account for proteins. The membrane permeability of the membrane barrier is calculated as though it were governed by free radial diffusion, as reduced by two large multiplicative factors. The first factor,  $n_{\text{pH}}$ , accounts for the reduced availability of the neutral form of fluoxetine, given the difference between the pK<sub>a</sub> of fluoxetine and that of the cell. The second factor,  $n_{\text{accum}}$ , is the reduction caused by binding to membrane lipids (Crank, 1975). The factor  $n_{\text{accum}} = (\text{lipid molarity in the shell}) / (\text{assumed fluoxetine-lipid } K_d)$  (Alberts et al., 2015). The latter  $K_d$  is the most important adjustable parameter (see below, Results; see Figs. 5C, 7L, Table 1).

Most classical analyses do not consider drug accumulation within the infinitely thin membrane barrier of zero volume. Therefore, we enhanced the classical simulation by including a routine that simultaneously calculates drug accumulation within a membrane shell of finite thickness and volume. The composition, thickness, and volume are exactly those used to compute the permeability of the membrane barrier above. Thus, the membrane shell has the lipid molarity and fluoxetine-lipid  $K_d$  described above and has a thickness of 10 nm (inner and outer radii at 7.495 and 7.505 μm, respectively). Fluoxetine accumulation is calculated by simply multiplying the [fluoxetine] within the membrane shell by  $n_{\text{accum}}$ . Fluoxetine accumulation does not deplete the total number of drug molecules. The inward-facing border of the membrane shell undergoes free diffusion with the next inward shell, as described for all other pairs of adjoining shells. The outer border of the membrane shell is

the membrane barrier, whose permeability is described above. In the simulated results, the waveform of drug concentration within the membrane shell is simultaneous with those in the cytoplasm, within ~50 ms.

This conceptual scheme is valid only if the concentration source and sink lie outside the membrane barrier, allowing the accumulation within the membrane shell to be influenced by the delayed permeation through the membrane barrier. A more complete version, also allowing sources and sinks within the cell, would include both a 5-nm-thick inner membrane shell and a 5-nm-thick outer membrane shell, flanking the membrane barrier.

The model was constructed in the graphical user interface (GUI) of MATLAB SimBiology (MathWorks). For our purposes, this interface has heuristic value; but it has the disadvantage that rate constants and shell volumes must be calculated externally. Therefore, we transferred the parameters manually to the GUI from the calculations and assumptions in an Microsoft Excel spreadsheet (Table 1). SimBiology then integrated the equations to produce drug molarity versus time in each spherical shell (see Figs. 5C, 7L). Both the SimBiology project (SBPROJ file) and the Excel spreadsheet may be downloaded from [https://github.com/lesterha/lesterlab\\_caltech](https://github.com/lesterha/lesterlab_caltech).

For our purposes, SimBiology itself has the following strengths: (1) It verifies consistency among the dimensions and units, and (2) it has robust routines for integrating stiff differential equations. SimBiology has the following limitations: (1) It cannot treat surface densities in a compartment of zero volume, and (2) its dosing routines cannot jump the concentration of a source or sink. Therefore, the wash-in and washout phases (see Figs. 5C, 7L) were simulated separately.

**Total cellular accumulation, intracellular bioavailability, and lipid binding.** Atorvastatin calcium salt, escitalopram oxalate, fluoxetine hydrochloride, lopinavir, and warfarin were obtained from Sigma-Aldrich at their highest degree of purity (≥98%). Atorvastatin and lopinavir were selected as reference compounds (Mateus et al., 2017), and warfarin was used as an internal standard. Atorvastatin, escitalopram, fluoxetine, lopinavir, and warfarin were made as stocks in DMSO (≥2 mM).

Total accumulation ratio (K<sub>p</sub>) was measured as described previously (Treyer et al., 2019) but at several time points. In DMEM with addition of L-glutamine and 10% FBS, human embryonic kidney 293 (HEK293) cells were seeded at passage 14 at 6 × 10<sup>5</sup> cells/ml in 24-well Corning CellBIND plates. At confluence, they were washed twice with HBSS and incubated with 200 μl of HBSS containing 0.5 μM of compound for 30–120 min at 100 rpm. At each time point, the medium was sampled before washing the cells with HBSS and extracting the intracellular compound using acetonitrile/water (60/40) for 15 min at 500 rpm. Protein content was quantified in representative wells using a Thermo Fisher Pierce BCA assay kit. Cellular volume (V<sub>cell</sub>) was calculated assuming 6.5 μl/mg protein (Treyer et al., 2018, 2019). A<sub>cell</sub> is the amount of compound in cells (in fmol). C<sub>medium</sub> is the concentration in the surrounding medium (in nM). Experiments were conducted in triplicate on three independent occasions. Compounds were quantified via ultra performance liquid chromatography tandem mass spectrometry (UPLC-MS). K<sub>p</sub>, the intracellular compound accumulation, was calculated according to the following:

$$K_p = \frac{A_{\text{cell}}/V_{\text{cell}}}{C_{\text{medium}}}.$$

Data were plotted using Prism 9.

Binding to lipid-coated beads ( $f_{\text{u,lipid}}$ ) was measured with TRANSILXL Intestinal Absorption Kit (catalog #TMP-0100-2096, Sovicell), as outlined in Treyer et al. (2019). Briefly, phosphatidylcholine-coated silica beads and 5 μM drug were incubated for 12 min, with orbital shaking. The beads were centrifuged at 750 rpm for 10 min before sampling from the supernatant. Experiments were conducted in triplicate at three independent occasions. Compounds were quantified by LC-MS/MS. The  $f_{\text{u,lipid}}$  metric, the fraction of unbound compound, was then calculated as outlined in Treyer et al. 2018, 2019. D<sub>L</sub>, an optimized dilution factor determined by minimizing the sum of the squared prediction errors (Microsoft Excel, Solver add-in), was used to scale  $f_{\text{u,lipid}}$  to  $f_{\text{u,cell}}$ , the predicted intracellular fraction of unbound compound, according to the following:

**Table 1. Values from a Microsoft Excel worksheet that calculates the parameters of the diffusion-binding model for neurons**

Compartment	Shell outer radius $\mu\text{m}$	Shell volume $\mu\text{m}^3$	pH Divisor $n_{\text{pH}}$	Binding divisor $n_{\text{accum}}$	First-order rate constants	Permeability	Lipid molarity in shell M	Assumed fluoxetine-lipid $K_d$ M
					$k_f = k_b = D_{\text{eff}}^*$ A/thickness $\mu\text{m}^3/\text{ms}$	Classical permeability $k = D_{\text{eff}}/\text{thickness } \mu\text{m}/\text{ms}$		
Cytoplasmic shells	0.5	0.52	1	1	1.26	0.4		
	1	3.67	1	1	5.03	0.4		
	1.5	9.95	1	1	11.31	0.4		
	2	19.37	1	1	20.11	0.4		
	2.5	31.94	1	1	31.42	0.4		
	3	47.65	1	1	45.24	0.4		
	3.5	66.50	1	1	61.58	0.4		
	4	88.49	1	1	80.42	0.4		
	4.5	113.62	1	1	101.79	0.4		
	5	141.90	1	1	125.66	0.4		
	5.5	173.31	1	1	152.00	0.4		
	6	207.87	1	1	181.00	0.4		
	6.5	245.57	1	1	212.37	0.4		
	7	286.41	1	1	246.30	0.4		
7.495	326.86	1	1	282.37	0.4			
Membrane shell	7.505	7.07	230	208	0.01	8.36E-06	0.416	2.00E-03
Membrane barrier		NA			0.01	8.36E-06		
Extracellular shells	8	373.98	1	1	324.95	0.4		
	8.5	427.78	1	1	363.17	0.4		
	9	481.19	1	1	407.15	0.4		
	9.5	537.74	1	1	453.65	0.4		
	10	597.43	1	1	502.65	0.4		
	10.5	660.26	1	1	554.18	0.4		
	11	726.23	1	1	608.21	0.4		
	11.5	795.35	1	1	664.76	0.4		
	12	867.60	1	1	723.82	0.4		
	12.5	943.00	1	1	785.40	0.4		
	13	1021.54	1	1	849.49	0.4		
	13.5	1103.22	1	1	916.09	0.4		
	14	1188.04	1	1	985.20	0.4		
	14.5	1276.01	1	1	1056.83	0.4		
15	1367.12	1	1	1130.97	0.4			
15.5	1461.36	1	1	1207.63	0.4			

See above, Materials and methods, Simulations of diffusion and binding. Another worksheet in the workbook calculates the model for HeLa cells. Several columns with intermediate calculations are hidden. The workbook, an XLSX file, is available at [https://github.com/lesterlab/lesterlab\\_caltech](https://github.com/lesterlab/lesterlab_caltech). The bidirectional rate constants  $k_f = k_b$  Govern the flux between each shell and the next larger shell (See above, Materials and methods, Simulations of diffusion and binding). The "Membrane shell" row represents the calculations contributing to both the permeability of the membrane barrier and fluoxetine accumulation in the membrane shell. In the membrane barrier, the diffusion constant is reduced by two multiplicative factors (See above, Materials and methods, Simulations of diffusion and binding). The factor,  $n_{\text{pH}}$ , accounts for the reduced availability of the neutral form of fluoxetine, given the difference between the calculated  $\text{pK}_a$  of fluoxetine (9.8) and that of the external solution (7.4). The factor  $n_{\text{accum}}$  is the (lipid molarity in the shell)/(assumed fluoxetine-lipid  $K_d$ ). The lipid molarity is calculated from the usual assumption that each membrane leaflet has a lipid density of 2.5 million molecules/ $\mu\text{m}^2$  (Alberts et al., 2015). The assumed fluoxetine-lipid  $K_d$  is the most important adjustable parameter. The value of 2.2 mM produces a half-time of 251 s and is consistent with the measured value of at  $\geq 100 \mu\text{M}$  (Treyer et al., 2019). In the worksheet for HeLa,  $K_d$  has the value of 22 mM. The membrane barrier comprises a set of two equal rate constants, as though it were physically located at 7.505  $\mu\text{m}$ . The "Membrane barrier" row gives the rate constants corresponding to the permeability of the membrane barrier. The value of  $n_{\text{accum}}$  in the "Membrane shell" row is also used to calculate accumulation in the membrane shell. Varying the assumed membrane shell thickness over a threefold range changed the simulated kinetics by  $< 10\%$  because the structure of the model has compensatory changes in several parameters.

$$f_{u,\text{cell}} = \frac{1}{D_L \cdot \left( \frac{1}{f_{u,\text{lipid}}} - 1 \right) + 1}$$

Intracellular bioavailability,  $F_{ic}$  (Mateus et al., 2017), was calculated from experimentally determined  $K_p$  and  $f_{u,\text{cell}}$  values using the following:

$$F_{ic} = K_p \cdot f_{u,\text{cell}}$$

UPLC-MS/MS analysis of sampled fluids was performed on a Waters Acquity UPLC coupled to a Waters Xevo TQ-S micro MS. Chromatographic separation was achieved using a Waters 1.7  $\mu\text{m}$  C18 BEH column measuring  $2 \times 50$  mm with a gradient of 5% to 95% mobile phase B (0.1% formic acid in 100% acetonitrile) in mobile phase A (0.1% formic acid in LC-MS grade water) over a run-time of 2 min. The flow rate was 0.7 ml/min and 7  $\mu\text{l}$  of sample was injected per run. In electrospray ionization positive (ESI+) mode, the UPLC-MS parameters listed in Table 2 were used. Data were preprocessed using Waters MassLynx and TargetLynx 4.2 software.

**Plasmid availability.** We have deposited plasmids with the following at Addgene: cDNAs for iFluoxSnFR (182808), iEscSnFR

(182807); pCMV(MinDis)-iFluoxSnFR\_PM (182816), pCMV(MinDis)-iEscSnFR\_PM (182813), pCMV(MinDis)-iFluoxSnFR\_cyto (182817), pCMV(MinDis)-iEscSnFR\_cyto (182814), pCMV(MinDis)-iFluoxSnFR\_ER (182815), pCMV(MinDis)-iEscSnFR\_ER (182812), pAAV9-hSyn-iFluoxSnFR\_PM (182822), pAAV9-hSyn-iEscSnFR\_PM (182819), pAAV9-hSyn-iFluoxSnFR\_cyto (182823), pAAV9-hSyn-iEscSnFR\_cyto (182820), pAAV9-hSyn-iFluoxSnFR\_ER (182821), pAAV9-hSyn-iEscSnFR\_ER (182818).

## Results

### Generation of iDrugSnFRs for escitalopram and fluoxetine

To generate iDrugSnFRs for SSRIs, we screened several SSRIs against a panel of biosensors that included our previously published biosensors based on the periplasmic binding protein (PBP) OpuBC (Bera et al., 2019; Shivange et al., 2019; Unger et al., 2020; Nichols et al., 2022) as well as intermediate constructs from their development process (Beatty et al., 2022). From this screen, we identified possible biosensors for fluoxetine and escitalopram. We chose sensors with

**Table 2. Mass spectrometry parameters for chemical detection of compounds used in HEK cell and lipid-coated bead assays**

Compound	Retention time (min)	Parent (m/z)	Daughter (m/z)	Cone voltage (V)	Dwell time (s)	Collision energy (V)
atorvastatin	1.54	559.3487	440.2340	14	0.164	20
escitalopram	1.25	325.0489	108.8380	22	0.025	26
fluoxetine	1.33	310.1700	148.0700	36	0.110	8
lopinavir	1.59	629.5000	155.1000	22	0.025	46
warfarin	1.50	309.1662	163.1476	34–40	0.110–0.025	15–16

m/z is mass/charge.

the lowest EC<sub>50</sub> for each drug as our starting protein for iDrugSnFR evolution.

We incrementally applied SSM to first- and second-shell amino acid positions within the binding pocket. We evaluated each biosensor and drug partner in lysate from *Escherichia coli* and carried forward the biosensor with the highest S-slope to the subsequent round. Figure 1 summarizes concentration–response relations for the optimized sensors. The escitalopram sensor, iEscSnFR, displayed EC<sub>50</sub> 4.5 ± 0.2 μM, ΔF<sub>max</sub>/F<sub>0</sub> 16 ± 0.3, and S-slope 3.6. The fluoxetine sensor, iFluoxSnFR, displayed EC<sub>50</sub> 8.7 ± 0.2 μM, ΔF<sub>max</sub>/F<sub>0</sub> 9.2 ± 0.1, and S-slope 1.1. (Fig. 1A).

### Specificity and thermodynamics of SSRI iDrugSnFRs

We characterized the specificity of purified SSRI iDrugSnFRs for their drug partners versus a panel of related antidepressants, antidepressant metabolites, and nicotinic agonists (Fig. 1B,C). The newly developed iDrugSnFRs showed some sensitivity to other antidepressants. iEscSnFR had greater fidelity for its drug partner, binding few drugs in our panel except for choline (EC<sub>50</sub> of 140 ± 20 μM, a value ~10-fold above endogenous levels; Zeisel et al., 1980; Schapiro et al., 1990; Vargas and Jenden, 1996; Fig. 1B). In contrast, iFluoxSnFR detected several compounds with EC<sub>50</sub> values between 32 and 170 μM, concentrations higher than those relevant for clinical purposes. iFluoxSnFR detected norfluoxetine, the breakdown product of fluoxetine, with an EC<sub>50</sub> of 63 ± 20 μM, a ninefold preference in binding for fluoxetine over norfluoxetine. iFluoxSnFR shows no binding to acetylcholine and choline (Fig. 1C). The relative selectivity of each biosensor for its partner compound indicates a structure/function relationship that differs from that of the interaction between hSERT and SSRIs.

We also performed concentration–response experiments with iEscSnFR and iFluoxSnFR against a panel of nine endogenous molecules and their precursors (Fig. 1D,E). Both iEscSnFR and iFluoxSnFR showed no response to any of the nine selected compounds above background.

To examine the thermodynamics of the iDrugSnFR–drug interaction, we conducted ITC binding experiments (Fig. 2A,B). The experimentally determined K<sub>d</sub> of iEscSnFR, 3.4 ± 0.1 μM, was within 1.5 times the experimentally determined EC<sub>50</sub> in purified protein (Fig. 2A,B).

When we attempted ITC with iFluoxSnFR and fluoxetine, the low aqueous solubility of fluoxetine resulted in distortion due to turbulent injections even after multiple attempts with various solvation schemes. Consequently, we performed ITC with *N,N*-dimethylfluoxetine (Fig. 2A,B). The experiments produced an experimentally determined K<sub>d</sub> of 28.1 ± 3.7 μM, approximately twice the experimentally determined EC<sub>50</sub> of iFluoxSnFR for *N,N*-dimethylfluoxetine (see Fig. 8). The ITC data imply that the EC<sub>50</sub> for fluorescence in iEscSnFR and iFluoxSnFR is dominated by the overall binding of the corresponding ligand.

### Stopped-flow experiments on SSRI iDrugSnFRs

We used a stopped-flow apparatus with millisecond resolution to measure the time course of fluorescent SSRI iDrugSnFR responses to step-like drug applications (Fig. 2C,D). These data show the trajectory of the ligand–sensor reaction as it relaxes to a new equilibrium after a sudden change in ligand concentration. For both sensors, most of the fluorescence change occurred within the first second with a monoexponential time course (Fig. 2C,D, top left). An additional smaller and slower exponential fluorescence increase continued over the next minute (Fig. 2C,D, top right).

In the 1 s stopped-flow experiments, the rate constants for the fluorescence relaxation (k<sub>obs</sub>) were a hyperbolic function of ligand concentration (Fig. 2C,D, bottom). For escitalopram binding to iEscSnFR, the zero-concentration intercept was 1.8 ± 0.1 s<sup>-1</sup>. The increased k<sub>obs</sub> was half-maximal at 7.7 ± 0.5 μM escitalopram. We fitted the data to a three-state kinetic mechanism: the apo state, a drug-bound nonfluorescent state, and a rate-limiting conformational change to the fluorescent state. These assumptions predicted an overall steady-state EC<sub>50</sub> of 1.7 ± 0.3 μM, compared with the value of 4.5 μM obtained with equilibrium concentration–response experiments on iEscSnFR (Fig. 1A). For fluoxetine binding to iFluoxSnFR, the zero-concentration intercept was 6.2 ± 1.5 s<sup>-1</sup>. The increased k<sub>obs</sub> was half-maximal at 7 ± 2 μM fluoxetine. The three-state mechanism predicted an overall steady-state EC<sub>50</sub> of 1.3 ± 0.7 μM, compared with the value of 8.7 μM obtained with equilibrium concentration–response experiments on iFluoxSnFR (Fig. 1A).

We have less complete measurements for the slower phase of the fluorescence increases. The half-maximal amplitudes and rate constants for the slower phases occurred at ligand concentrations in the same concentration range as those for the faster phase. This observation is consistent with the suggestion that the intense excitation beam in the stopped-flow experiments produced further photoactivation of the fluorescent state.

### Characterization of SSRI iDrugSnFRs in primary mouse hippocampal culture

We examined the subcellular pharmacokinetics of the SSRIs in primary mouse hippocampal neurons transduced with AAV vectors encoding the appropriately targeted iDrugSnFRs. The SSRI iDrugSnFRs were targeted to the PM (iDrugSnFR<sub>PM</sub>), the endoplasmic reticulum (iDrugSnFR<sub>ER</sub>), or the cytoplasm (iDrugSnFR<sub>cyto</sub>) as previously described (Bera et al., 2019; Shivange et al., 2019; Nichols et al., 2022). Spinning disk confocal microscopy showed targeting to the intended organelle or compartment (Fig. 3). ER-targeted biosensor was retained in the ER (Bera et al., 2019; Shivange et al., 2019; Nichols et al., 2022). iDrugSnFR targeted to the PM showed correct localization, with some iDrugSnFR observed in the cell interior (most likely as part of the cellular membrane trafficking system or inclusion bodies). The cytoplasm-targeted constructs appeared in both soma and dendrites.

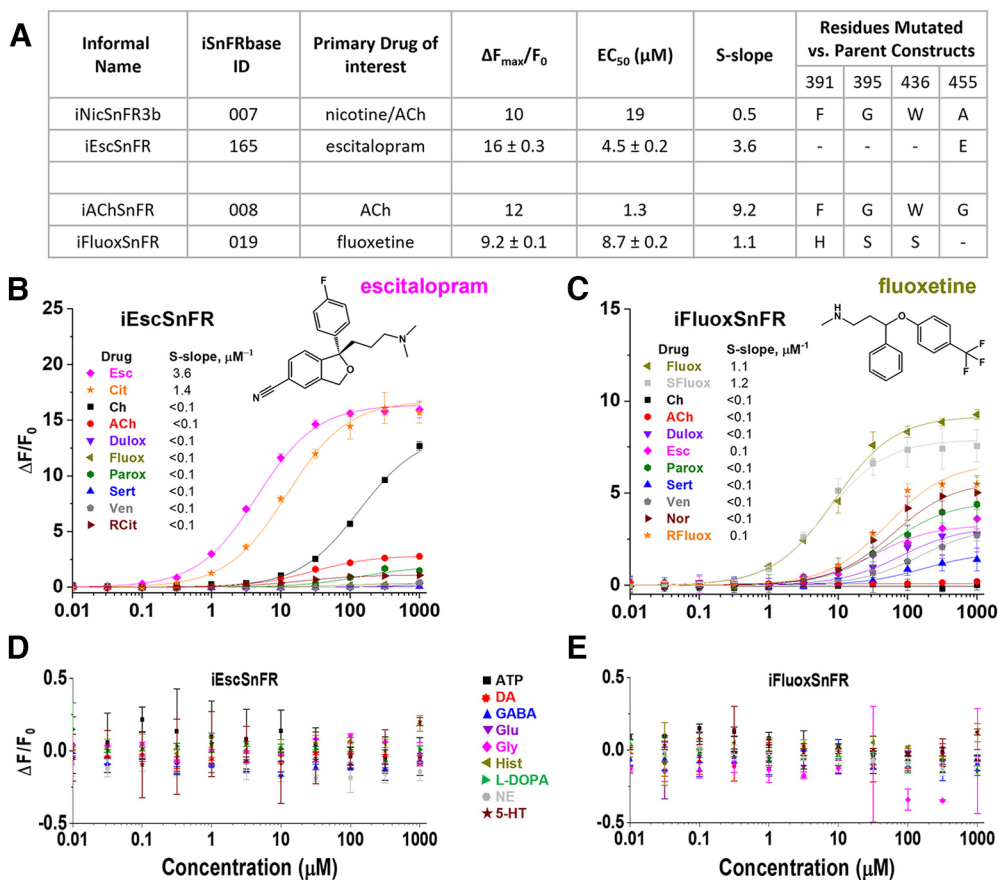


**Figure 1.** SSRI iDrugSnFR naming, residues mutated, and concentration–response relations. **A**, End points of SSRI iDrugSnFR development and concentration–response relations versus parent constructs. Data for iAChSnFR from Borden et al. (2019); data for iNicSnFR3b from Shivange et al. (2019). **B**, **C**, Concentration–response relations of purified iEscSnFR and iFluoxSnFR versus a drug panel. Ch, choline; ACh, acetylcholine; Dulox, duloxetine; Esc, escitalopram; Fluox, racemic fluoxetine; Parox, paroxetine; Sert, sertraline; Ven, venlafaxine; RCit, R-(+)-citalopram; Cit, racemic citalopram; Nor, norfluoxetine; RFluox, R-(+)-fluoxetine; SFluox, S(-)-fluoxetine. Inset, Relevant S-slope values for each iDrugSnFR. Dashed lines indicate concentration–response relations that did not approach saturation for the concentration ranges tested; therefore, EC<sub>50</sub> and  $\Delta F_{\max}/F_0$  could not be determined. iEscSnFR (**B**) shows preference for escitalopram over other SSRIs, with measurable binding to choline. iFluoxSnFR (**C**) shows a preference for racemic fluoxetine but also shows modest responses to other SSRIs. **D**, **E**, iEscSnFR (**D**) and iFluoxSnFR (**E**) shows little or no fluorescence response to all endogenous molecules tested. DA, dopamine; Glu, glutamate; Gly, glycine; Hist, histamine; L-DOPA, levodopa; NE, norepinephrine; 5-HT, serotonin.

We then performed concentration–response experiments in primary mouse hippocampal culture using wide-field fluorescence imaging with each iDrugSnFR and its drug partner, sampling a range of concentrations approximately an order of magnitude above and below the EC<sub>50</sub> as determined for the purified protein (Fig. 4, Movies 1, 2, 3, and 4). iEscSnFR showed a robust response to escitalopram at the PM and the ER across a range of concentrations from 0.1 to 31.6  $\mu\text{M}$ , and the speed was nearly limited by solution exchanges; there was a clear return to baseline fluorescence after each drug application on the order of seconds (Fig. 4A). A maximum  $\Delta F/F_0$  value of  $\sim 2$  was reached at 31.6  $\mu\text{M}$  with the iEscSnFR\_ER construct. We also observed a 10% higher  $\Delta F/F_0$  in the \_ER construct versus the \_PM construct in concentrations above 1  $\mu\text{M}$ , a phenomenon we had not encountered in any of our previous work.

In contrast, both the iFluoxSnFR\_ER and iFluoxSnFR\_PM constructs detected fluoxetine across a range of concentrations, but after 60 s of drug application, the  $\Delta F/F_0$  had not begun to plateau to a maximum value at concentrations of 1  $\mu\text{M}$  and higher (Fig. 4C). Therefore, responses to fluoxetine increases and decreases were much slower than solution changes for both constructs, on the order of hundreds of s. We also observed that the  $\Delta F/F_0$  of iFluoxSnFR\_ER was  $\sim$ twofold higher than iFluoxSnFR\_PM at concentrations of 3.16  $\mu\text{M}$  and higher.

Concentration–response experiments in primary hippocampal culture with iDrugSnFR\_cyto constructs demonstrated washout dynamics for escitalopram and fluoxetine similar to those obtained when the sensor was targeted to the PM and ER (Fig. 4B,D).

To further examine the extended kinetics of fluoxetine we observed with iFluoxSnFR, we recorded the fluorescence waveforms for fluoxetine at 1  $\mu\text{M}$  with an extended application time of 10 min and a washout time of 12 min (Fig. 5A). For the PM, the kinetics clearly showed two components. The faster component represented  $\sim 10\%$  of the total change and is indistinguishable from the solution change. The slower component had time constants of 200–300 s for both the wash-in and washout in iFluoxSnFR\_PM as well as in iFluoxSnFR\_ER. After a 12 min washout, both the iFluoxSnFR\_PM and \_ER constructs neared baseline fluorescence, indicating that full washout of fluoxetine can be achieved, but on a time scale nearly a log unit slower than for drugs such as nicotine and ketamine and two times slower than cytosine (Bera et al., 2019; Shivange et al., 2019; Muthusamy et al., 2022; Nichols et al., 2022).

To confirm that the iFluoxSnFR\_PM and \_ER constructs functioned as expected, and to ensure that the extended kinetics of fluoxetine we observed in primary hippocampal culture was not the result of idiosyncratic biosensor function or folding in neurons, we tested iFluoxSnFR\_PM and iFluoxSnFR\_ER versus

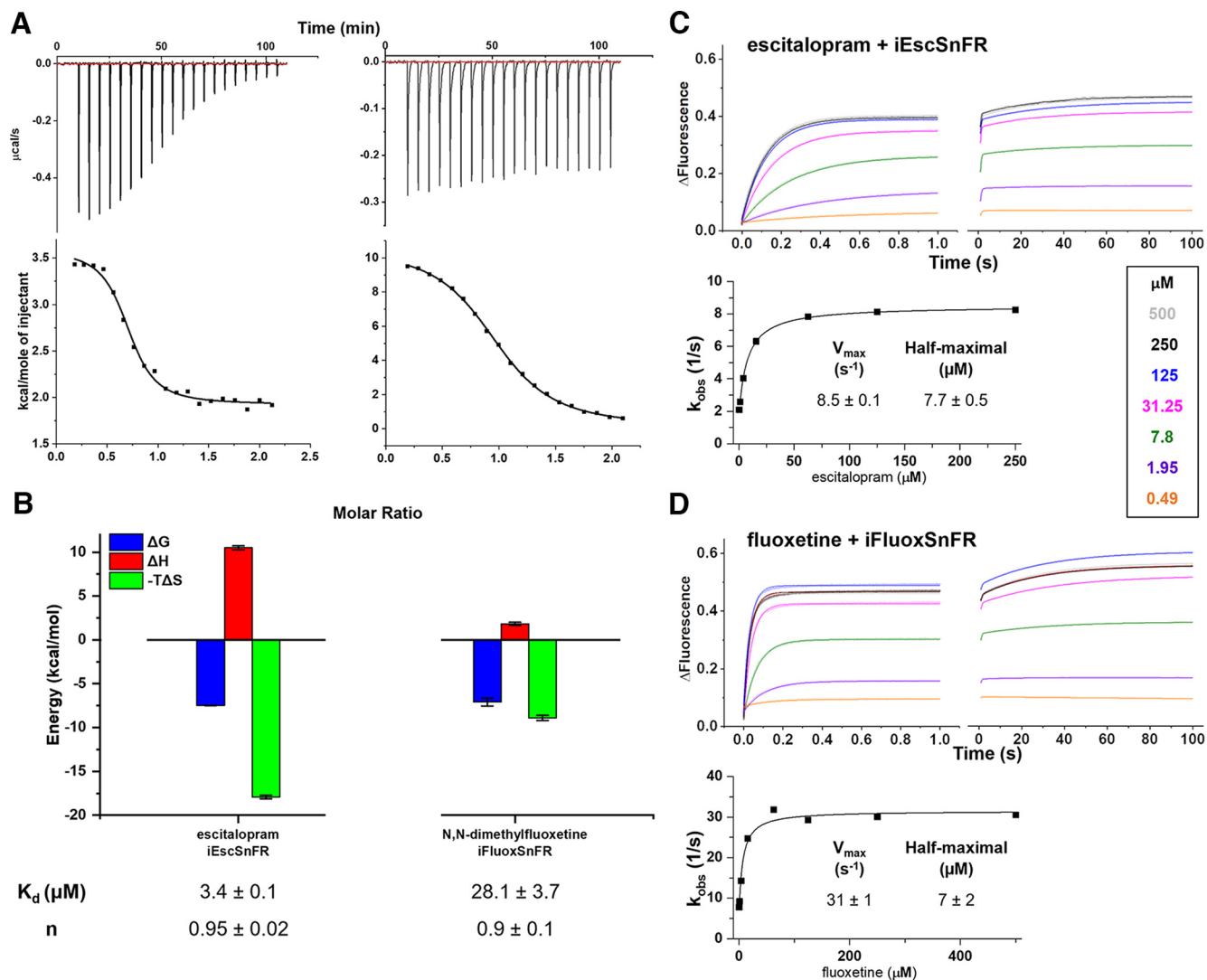


**Figure 2.** Thermodynamic and kinetic profiles of purified SSRI iDrugSnFR proteins. **A**, ITC traces and fits. Top row, Exemplar heat traces of iEscSnFR paired with escitalopram and iFluoxSnFR paired with *N,N*-dimethylfluoxetine as obtained by ITC. The heats for iEscSnFR and iFluoxSnFR were endothermic. Bottom row, The resulting fits for each iDrugSnFR:drug pair from the integrated heats comprising each series of injections. **B**, Energy calculations from ITC traces and fits. Both iDrugSnFRs show exergonic reactions, but the relative enthalpic and entropic contributions differ. Affinity ( $K_d$ ) and occupancy ( $n$ ) were also calculated. Data are from three separate runs. Mean  $\pm$  SEM. **C**, **D**, Stopped-flow fluorescence data for various concentrations of (**C**) iEscSnFR and (**D**) iFluoxSnFR recorded for periods of 1 and 100 s, at sampling rates of 1 ms and 1 s, respectively. Fluorescence was activated at time 0 by mixing agonist and sensor protein as noted. iEscSnFR and iFluoxSnFR data are fits to single exponentials. Plots of the exponential rate constants versus [agonist]s are included for the 1 s data.

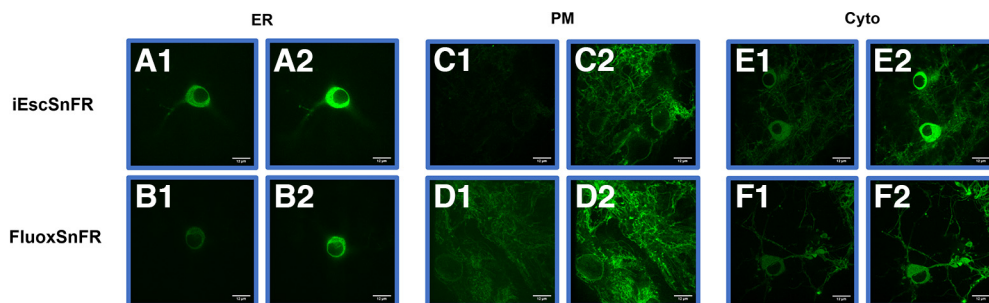


**Figure 3.** Spinning disk laser scanning confocal inverted microscope images of SSRI iDrugSnFRs in primary mouse hippocampal neurons. **A1–B2**, ER-targeted constructs of iEscSnFR and iFluoxSnFR are shown before (**A1**, **B1**) and during (**A2**, **B2**) exposure to each drug partner at  $10 \mu\text{M}$ . ER-targeted iDrugSnFRs show the eponymous reticulated pattern, and fluorescence is excluded from the nucleus. **C1–D2**, PM-targeted constructs of the same iDrugSnFRs are shown before (**C1**, **D1**) and during (**C2**, **D2**) drug introduction. Localization in the PM is robust, with some minimal puncta that may represent inclusion bodies or internal transport. **E1–F2**, Cytoplasm-targeted constructs of iEscSnFR and iFluoxSnFR are shown before (**E1**, **F1**) and during (**E2**, **F2**) exposure to each drug partner. Cytoplasm-targeted iDrugSnFR is expressed in the soma (excluding the nucleus) and the dendrites.

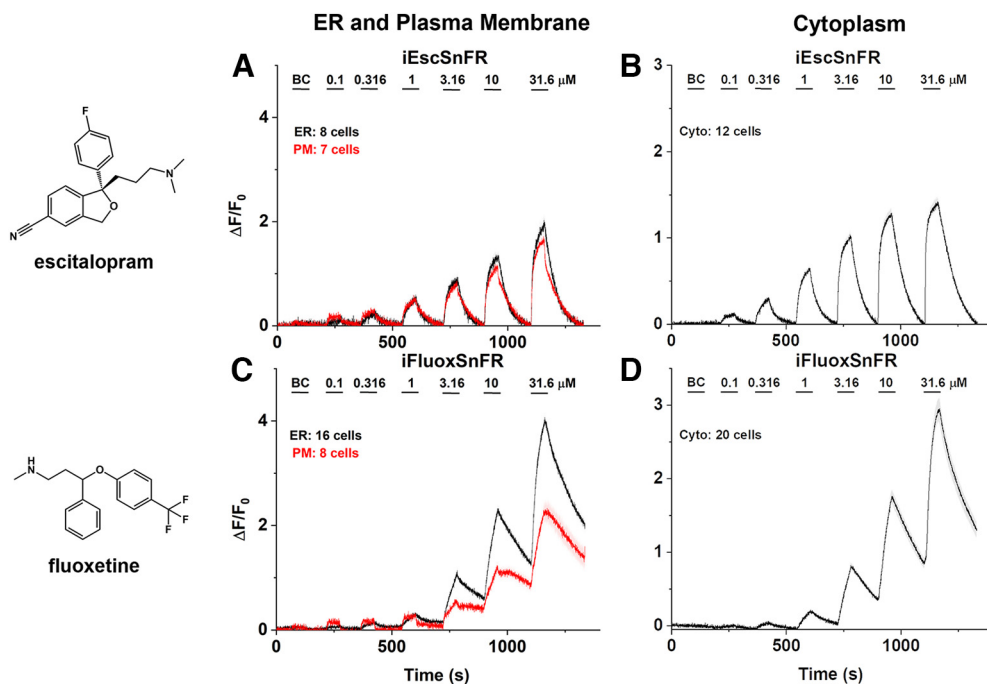
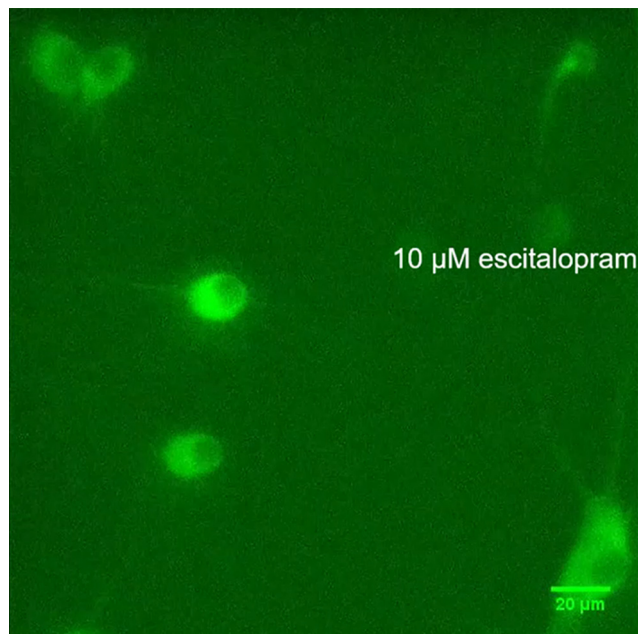
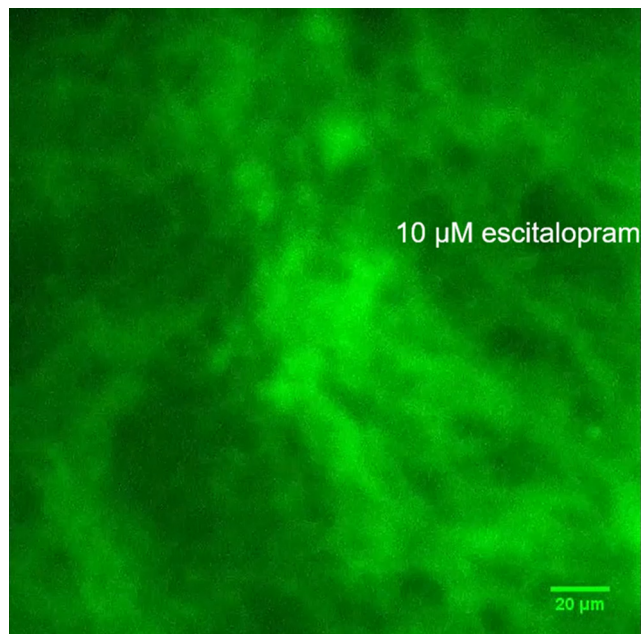


**Figure 4.** SSRI iDrugSnFR concentration–response relations in primary hippocampal culture. *A–D*, Each iDrugSnFR detects its drug partner at the ER, PM, or cytoplasm (cyto) of primary hippocampal culture at the concentrations sampled. BC, Buffer control. SEM of data are indicated by semitransparent shrouds around traces where trace width is exceeded. Drugs were applied for 60 s pulses at 120–150 s intervals. *A, B*, iEscSnFR detects escitalopram, approaching a plateau during the application, then returns to baseline fluorescence during the washout at all targeted locations. *C, D*, iFluoxSnFR detection of fluoxetine has not yet reached a plateau during the application, then shows an incomplete washout with no return to baseline fluorescence during the washout period in every targeted location.



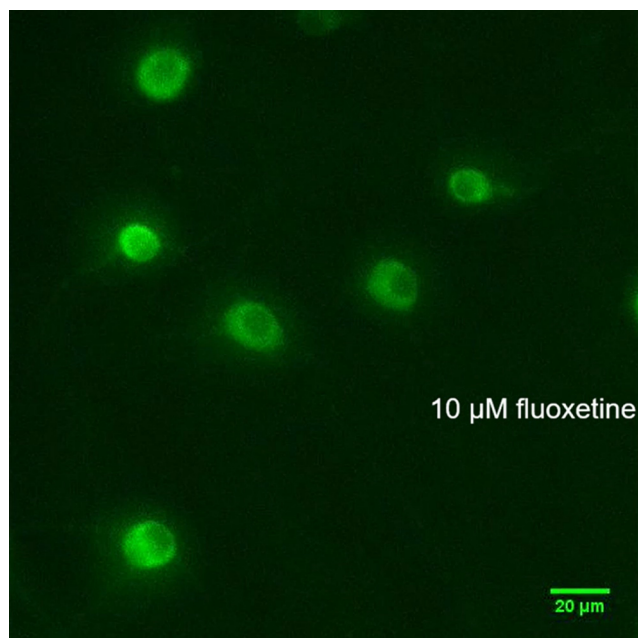
**Movie 1.** iEscSnFR\_ER concentration–response relations in primary mouse hippocampal culture. The escitalopram concentrations are shown. The scale bar is shown. The video is 25-fold faster than real time. [View online]



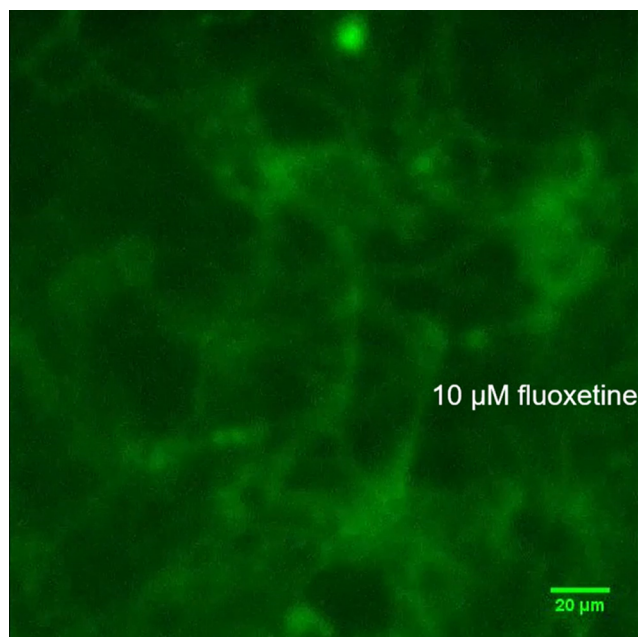
**Movie 2.** iEscSnFR\_PM concentration–response relations in primary mouse hippocampal culture. The escitalopram concentrations are shown. The scale bar is shown. The video is 25-fold faster than real time. [View online]

escitalopram. iFluoxSnFR binds escitalopram in the same concentration range as fluoxetine (although right shifted and with lower  $\Delta F/F_0$ ; Fig. 1C). After viral transduction of iFluoxSnFR\_PM and iFluoxSnFR\_ER, we performed time-resolved imaging for pulses of 0.1–31.6  $\mu\text{M}$  escitalopram

(Fig. 5B). These escitalopram waveforms resembled those of iEscSnFR detection of escitalopram in primary mouse hippocampal culture (Fig. 4A), confirming that iFluoxSnFR\_ER and \_PM function as expected. Thus, the slower kinetics for iFluoxSnFR\_ER and iFluoxSnFR\_PM arise from a property



**Movie 3.** iFluoxSnFR\_ER concentration–response relations in primary mouse hippocampal culture. The fluoxetine concentrations are shown. The scale bar is shown. The video is 25-fold faster than real time. [View online]



**Movie 4.** iFluoxSnFR\_PM concentration–response relations in primary mouse hippocampal culture. The fluoxetine concentrations are shown. The scale bar is shown. The video is 25-fold faster than real time. [View online]

inherent to the interaction between fluoxetine and the primary hippocampal culture.

### Estimating fluoxetine accumulation in the neuronal membrane

That the fluoxetine signals show time constants of 200–300 s at all three locations (PM, ER, and cytoplasm) led us to suspect the existence of a local binding site or sites that delay the appearance and disappearance of fluoxetine near neurons. A

related phenomenon is termed buffered diffusion (Armstrong and Lester, 1979).

We based our analysis on the unusually high pharmacokinetically defined volume of distribution exhibited by all SSRIs (see above, Introduction). Basic compounds can accumulate within the body via two major mechanisms: drug partitioning into membrane lipids and acid trapping within low-pH organelles (Smith et al., 2012).

We first turned our attention to drug partitioning into membrane lipids. Membrane partitioning should be distinguished from the more familiar, readily modeled fact that the protonated, charged species permeates membranes much more slowly than the uncharged, neutral species. Because both escitalopram and fluoxetine have calculated  $pK_a \sim 9.8$ , the charge-dominated effect is expected to decrease the effective diffusion constant ( $n_{pH}$ ) by at least two orders of magnitude (Yu et al., 2016).

Previous studies show how membrane partitioning of basic molecules plays a role in some molecular and cellular bases of the classical volume of distribution (Loryan et al., 2013; Mateus et al., 2014; Treyer et al., 2019). The nitrogen interacts with the phospholipid head groups, whereas the less polar moieties interact with the fatty acid tails (Mateus et al., 2014; Kapoor et al., 2019). The equilibrium parameters of such accumulation have been estimated by direct measurements on membrane-coated beads (see also below), by ITC, and by perturbation of gramicidin gating (Kapoor et al., 2019; Treyer et al., 2019). However, the kinetics of this accumulation are relatively unstudied and may be revealed for the first time by measurements reported in this paper (Figs. 4, C and D, and 5A).

The iFluoxSnFR measurements did show that locally measured SSRI concentrations eventually reach the applied concentration; the novel observation is that the approach to steady-state at the PM required several hundred seconds. We were able to simulate these delays (Fig. 5C) only by assuming that the extracellular-facing iFluoxSnFR\_PM measures, at least partially, the membrane-bound fluoxetine as it increases or decreases in response to step changes in the externally applied solutions. For previously reported PM-anchored iDrugSnFRs, the measurements were dominated by the free concentration in the extracellular aqueous phase (Bera et al., 2019; Shivange et al., 2019; Muthusamy et al., 2022; Nichols et al., 2022). Similarly, for membrane-excluded quaternary SSRI derivatives, the PM-anchored SSRI iDrugSnFRs also measured the aqueous concentrations of the drugs (see Figs. 8, 9). We suggest that the unique signals produced by fluoxetine at PM-localized iFluoxSnFR arise from two facts. First, if the anomalously high volume of distribution arises from the membrane accumulation, then this accumulation exceeds the aqueous concentration by orders of magnitude (the next paragraph gives an estimate). Second, PBPs from bacteria and archaea are specialized to transfer the ligand directly to membrane-embedded transporters that are adjacent (within just a few angstroms) to their PBP binding site (Scheepers et al., 2016; Nguyen et al., 2018; also PDB entries 2ONK, 4TQU, 2R6G, 6CVL, 4FI3, 5B58), in contrast to the several- $\mu\text{m}$ -thick unstirred layer inferred from ITC measurements on the fluoxetine-lipid interaction (Kapoor et al., 2019).

Our data yielded an estimate of membrane partitioning. With the unique sensing assumption discussed above, we modeled the fluoxetine measurements by assuming that the effective diffusion coefficient is reduced further by lipid binding within the membrane (Crank, 1975). Table 1 gives our assumptions for the better-characterized underlying parameters. The most important

adjustable parameter is the binding constant  $K_d$  for lipid-fluoxetine binding. The only available measurement is at least  $100 \mu\text{M}$  (Mateus et al., 2013). Because we treat membrane permeation as a single first-order process whose kinetics are orders of magnitude slower than diffusion in the cytoplasm and extracellular solution, the simulation predicts exponential kinetics. The experimentally measured time constant of 200–300 s (Fig. 5A) was explained by a  $K_d$  of 2.2 mM. The extent of membrane accumulation is therefore (lipid molarity in the shell)/(fluoxetine-lipid  $K_d$ ), or 181-fold higher than the free solution value of fluoxetine.

### Uninformative measurements on fluoxetine accumulation in acidic vesicles

Acid trapping within low-pH organelles has been suggested for nicotine, antipsychotics, ketamine, and other weakly basic cationic drugs (Lester et al., 2009; Tischbirek et al., 2012; Mateus et al., 2013; Lester et al., 2015; Tucker et al., 2015; Govind et al., 2017). To simulate fluoxetine accumulation within synaptic vesicles, we employed a theoretical model that includes the  $pK_a$  of the drug, the  $\text{LogP}$  of the neutral and protonated form, the diameter of the vesicle, and corrections for ionic strength (Fig. 6A; Trapp et al., 2008). The simulations suggest that the accumulation occurs on a time scale of several hundred seconds, amounting to  $\sim 100$ -fold increase over the concentration in the extracellular solution. Because present iDrugSnFRs do not function at pH less than  $\sim 6.5$  (Bera et al., 2019; Shivange et al., 2019; Muthusamy et al., 2022), we could not measure SSRI directly within the lumen of acidic vesicles. We therefore resorted to indirect measures—transient modification of the signals measured in other compartments.

We first tested for vesicular accumulation by blocking the vesicular proton pump with folimycin. We found little to no effect of such blockade (Fig. 6B). Some spinning disk confocal microscope images revealed that the PM-targeted iDrugSnFRs had brightest signals near synapses (Fig. 3D1,D2 is an example); therefore, we sought a method to test for accumulation within synaptic vesicles. The solution changes on the spinning-disk confocal microscope required several minutes—too slow to reveal the expected temporal distortions. The perfusion system in the wide-field fluorescent microscope could change solutions in  $\sim 1$  s, but the spatial resolution of the  $40\times$  lens was several micrometers—insufficient to reveal individual synaptic sites. Therefore, in time-resolved images with the wide-field microscope, we compared data from regions of interest (ROIs) that included primarily neurites or primarily somata (Fig. 6C). We found no significant differences between the two sets of ROIs (Fig. 6D).

Because the endolysosomal compartment represents only  $\sim 1\%$  of the cytosol, drug accumulation in synaptic vesicles or other acidic vesicles is expected to contribute little or no temporal distortion of the signals we measured. Therefore, the set

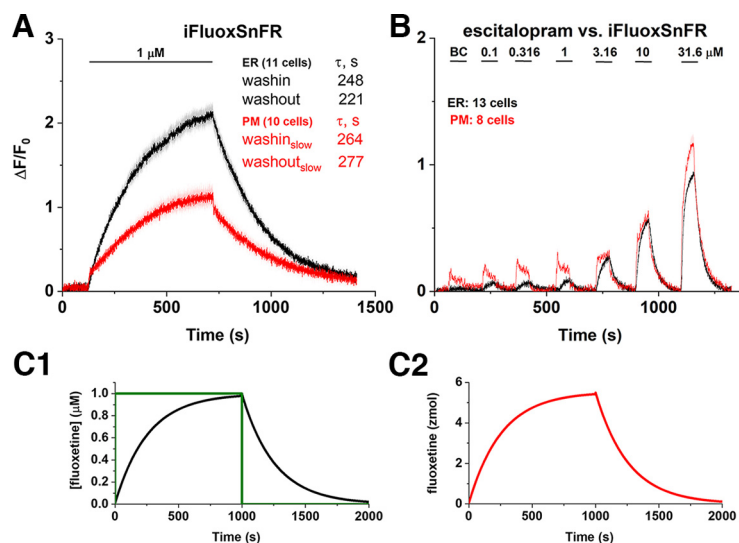


**Figure 5.** Further analysis of fluoxetine kinetics in primary hippocampal neurons. **A**, Traces of fluorescence responses during exposure to  $1 \mu\text{M}$  fluoxetine with iFluoxSnFR. BC, Buffer control. SEM of data are indicated by semitransparent shrouds around traces where trace width is exceeded. A relatively long application (600 s) allowed ER- and PM-targeted iFluoxSnFR detection of  $1 \mu\text{M}$  fluoxetine to approach a maximum  $\Delta F/F_0$ . A slightly longer (720 s) washout allowed a return to baseline fluorescence for both ER- and PM-targeted iFluoxSnFR. Time constants for the slower phase are given as  $\tau$  (s). **B**, A control experiment, imaging concentration–response relations for escitalopram against iFluoxSnFR. SEM of data are indicated by semitransparent shrouds around traces where trace width is exceeded. iFluoxSnFR detects escitalopram at both the PM and ER. Escitalopram enters and exits the ER with a return to baseline fluorescence during the washout, a direct contrast to the behavior of fluoxetine as detected by iFluoxSnFR. **C**, Simulations of fluoxetine in the extracellular space, plasma membrane, and cytoplasm of a spherical cell. **C1**, The green trace gives the applied (damped) [fluoxetine] in a shell  $11.5 \mu\text{m}$  from the center of the cell. At a radius of  $11.5 \mu\text{m}$  in the extracellular solution, the concentration is stepped from 0 to  $1 \mu\text{M}$  for 1000 s; the concentration is then stepped back to zero (green trace). The concentrations in all extracellular shells (between the  $11.5 \mu\text{m}$  shell and the PM shell at  $7.5 \mu\text{m}$  radius) equilibrate within  $\sim 50$  ms and are indistinguishable from the applied concentration on this time scale. The black trace gives the cytoplasmic [fluoxetine] within the shell of outer radius of  $7.495 \mu\text{m}$ , 10 nm below the plasma membrane. The concentrations in all other intracellular shells show a dispersion of  $\sim 50$  ms and are indistinguishable from the black trace on this time scale. The intracellular [fluoxetine] resembles that of **A**. **C2**, The moles of fluoxetine bound within the simulated membrane shell. With the parameters given in Table 1, the time course of PM-bound fluoxetine is indistinguishable from that of intracellular [fluoxetine] and resembles that of **A** (see above, Materials and Methods; Table 1).

of experiments to test for fluoxetine accumulation in acidic vesicles has given uninformative results.

### Characterization of SSRI iDrugSnFRs in HeLa cells

In light of the surprisingly slow kinetics from imaging iFluoxSnFR in primary cultured neurons, we examined the subcellular pharmacokinetics of the SSRI in a transfected mammalian cell line. The SSRI iDrugSnFRs were targeted to the PM (iDrugSnFR<sub>PM</sub>) or the ER (iDrugSnFR<sub>ER</sub>) as previously described (Bera et al., 2019; Shivange et al., 2019; Muthusamy et al., 2022; Nichols et al., 2022). We also assembled iEscSnFR and iFluoxSnFR constructs targeted to the cytoplasm (iEscSnFR<sub>cyto</sub> and iFluoxSnFR<sub>cyto</sub>) for use in HeLa cells. To examine the localization of the three constructs at higher optical resolution, we imaged HeLa cell cultures using a spinning disk laser scanning inverted confocal microscope (Fig. 7A–C,F–H). Localization of the biosensor resembled previously described iDrugSnFR<sub>PM</sub> and <sub>ER</sub> constructs (Bera et al., 2019; Shivange et al., 2019; Muthusamy et al., 2022; Nichols et al., 2022) and the localization pattern of iEscSnFR and iFluoxSnFR in primary hippocampal culture imaging (Fig. 3). The <sub>cyto</sub> construct was excluded from the nucleus but otherwise showed a relatively featureless intracellular pattern.

We performed concentration–response experiments in HeLa cells using wide-field fluorescence imaging with each iDrugSnFR

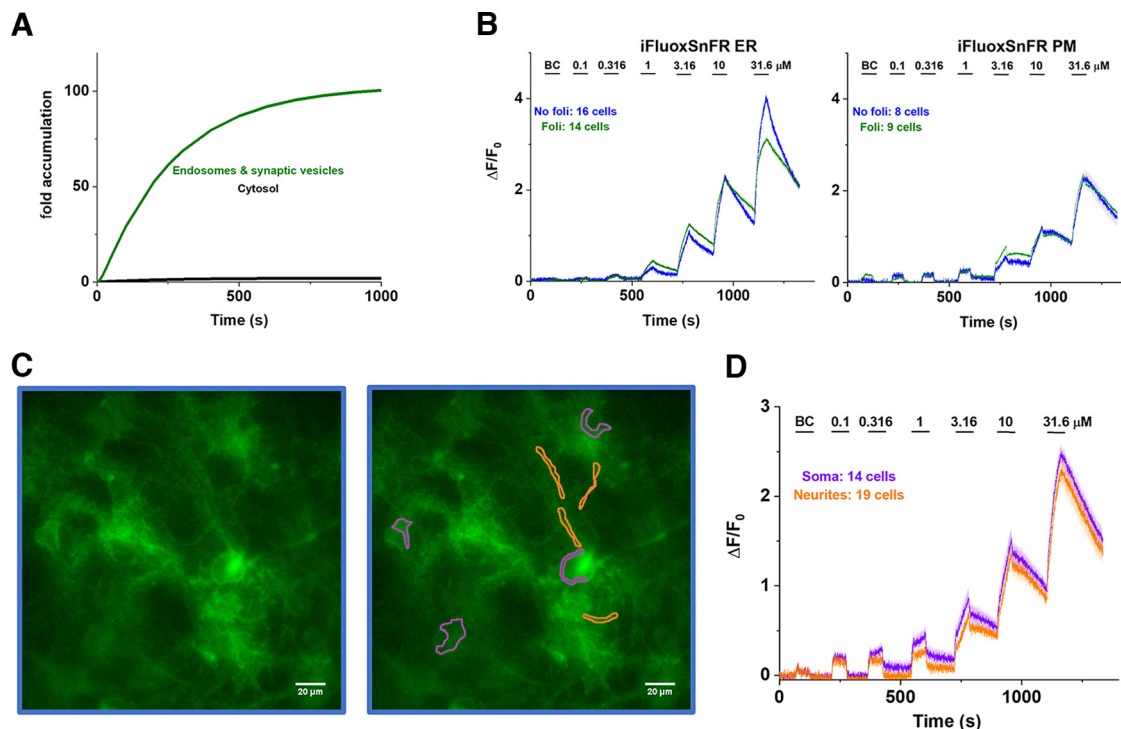


**Figure 6.** Predictions and experiments on acid trapping of fluoxetine. **A**, Predicted accumulation of fluoxetine in synaptic vesicles and/or endosomes (green, pH 5.5) versus cytosol (black, pH 7.2). The extracellular solution has an assumed pH of 7.4. The calculations were performed according to the theory of Trapp et al. (2008). We assume the following: The cell and vesicles have a diameter of 8  $\mu\text{m}$  and 100 nm, respectively; fluoxetine has a  $\text{pK}_a$  of 9.8; the neutral form has  $\text{LogP}$  of 4.1; and the charged form has a 7.5 log unit smaller  $\text{LogP}$ . The Excel workbook that performs the calculations is posted at [https://github.com/lesterha/lesterlab\\_caltech](https://github.com/lesterha/lesterlab_caltech). **B**, Pretreatment of primary hippocampal neurons with 80 nM folimycin (abbreviated Foli) does not substantially alter the concentration–response relations or waveforms for iFluoxSnFR against fluoxetine versus untreated neurons in parallel experiments. **C**, A typical field of cultured hippocampal neurons expressing iFluoxSnFR\_PM. Orange outlines show ROIs for four neurite regions; purple lines show ROIs for four somatic regions. **D**, Mean  $\pm$  SEM waveforms for all ROIs analyzed. There was no substantial difference between neurite and somatic fluoxetine responses.

and its drug partner, applying the same concentrations as in the neuronal cell culture experiments (Fig. 7D,E,I,J). Compared with the cultured neuron experiments, the HeLa cell experiments showed larger  $\Delta\text{F}/\text{F}_0$  across all concentrations sampled for the \_PM, \_ER, and \_cyto constructs (Fig. 4), primarily because the very thin HeLa cells have little endogenous fluorescence and therefore comparatively small  $\text{F}_0$ . iEscSnFR showed a robust response to escitalopram at the PM, ER, and cytoplasm of HeLa cells across a range of concentrations from 0.1 to 31.6  $\mu\text{M}$ , and the speed was nearly limited by solution changes. At 31.6  $\mu\text{M}$ , the PM had  $\Delta\text{F}/\text{F}_0$  of  $\sim 2.75$ , whereas the ER had  $\Delta\text{F}/\text{F}_0$  of  $\sim 2.5$ ; at concentrations below this value, the ER had  $\sim 30$ – $80\%$  of the PM signal, which indicated a difference in membrane crossing (Fig. 7D). The \_cyto construct had a maximal  $\Delta\text{F}/\text{F}_0$  of  $\sim 2$  at 31.6  $\mu\text{M}$ .

The iFluoxSnFR\_PM construct detected fluoxetine across a range of concentrations, reaching a maximum  $\Delta\text{F}/\text{F}_0$  of  $\sim 3.25$  at 31.6  $\mu\text{M}$ , with the \_ER construct displaying  $\sim 50$ – $80\%$  of the signal seen in the PM construct (Fig. 7I). The \_cyto construct had a maximal  $\Delta\text{F}/\text{F}_0$  of  $\sim 2.25$  at 31.6  $\mu\text{M}$ . iFluoxSnFR targeted to the PM, cytoplasm, or ER in HeLa cells showed wash-in and washout kinetics that were slower than the solution changes but  $\sim 10$ -fold more rapid than in hippocampal cultures. At 1  $\mu\text{M}$  fluoxetine (Fig. 7K), the \_ER and \_cyto constructs displayed single exponential kinetics as in the neuronal cultures. The iFluoxSnFR\_PM construct showed two phases during the wash-in and washout, like the same construct expressed in neurons. As in neurons, the faster phase was indistinguishable from the solution change; but it accounted for  $\sim 80\%$  of the waveform in contrast to the  $\sim 10\%$  in neurons.

We simulated the slower phase of fluoxetine kinetics in HeLa cells using the diffusion-binding model (Fig. 7L). We assumed that fluoxetine accumulation in the membrane is governed by a fluoxetine-lipid  $\text{K}_d$  of 22 mM, or  $\sim 10$ -fold weaker than in hippocampal neurons. This assumption of weaker membrane accumulation may also explain how iFluoxSnFR\_PM signal is dominated by the [fluoxetine] in the extracellular solution, with only a small contribution from fluoxetine accumulated in the PM.

#### Cellular experiments with impermeant SSRI derivatives

We performed concentration–response experiments for purified iEscSnFR and iFluoxSnFR with quaternary derivatives of these two drugs (Fig. 8). In solutions with purified iDrugSnFRs, the  $\Delta\text{F}/\text{F}_0$  of iEscSnFR with *N*-methylescitalopram and escitalopram was nearly identical at  $\sim 16$ , but iEscSnFR had an  $\sim$ twofold lower  $\text{EC}_{50}$  for *N*-methylescitalopram at  $1.8 \pm 0.2 \mu\text{M}$  (Fig. 8A). iFluoxSnFR detected *N,N*-dimethylfluoxetine with  $\Delta\text{F}/\text{F}_0$  of  $5.0 \pm 0.1$ , which was lower than that for fluoxetine ( $6.6 \pm 0.1$ ). The  $\text{EC}_{50}$  of iFluoxSnFR for *N,N*-dimethylfluoxetine was  $14 \pm 0.4$  versus the  $\text{EC}_{50}$  of  $8.3 \pm 0.6 \mu\text{M}$ , an  $\sim$ twofold shift in affinity (Fig. 8B).

In imaging-based concentration–response experiments with the quaternary SSRI derivatives in primary mouse hippocampal culture, the speed of the wash-in and washout phases was nearly limited by solution changes for both iEscSnFR\_PM and iFluoxSnFR\_PM (Fig. 8C,D). The application of 31.6  $\mu\text{M}$  SSRI following the quaternary SSRI dosing (designed to act as a control) exhibited a kinetic profile resembling the equivalent concentration in previous concentration–

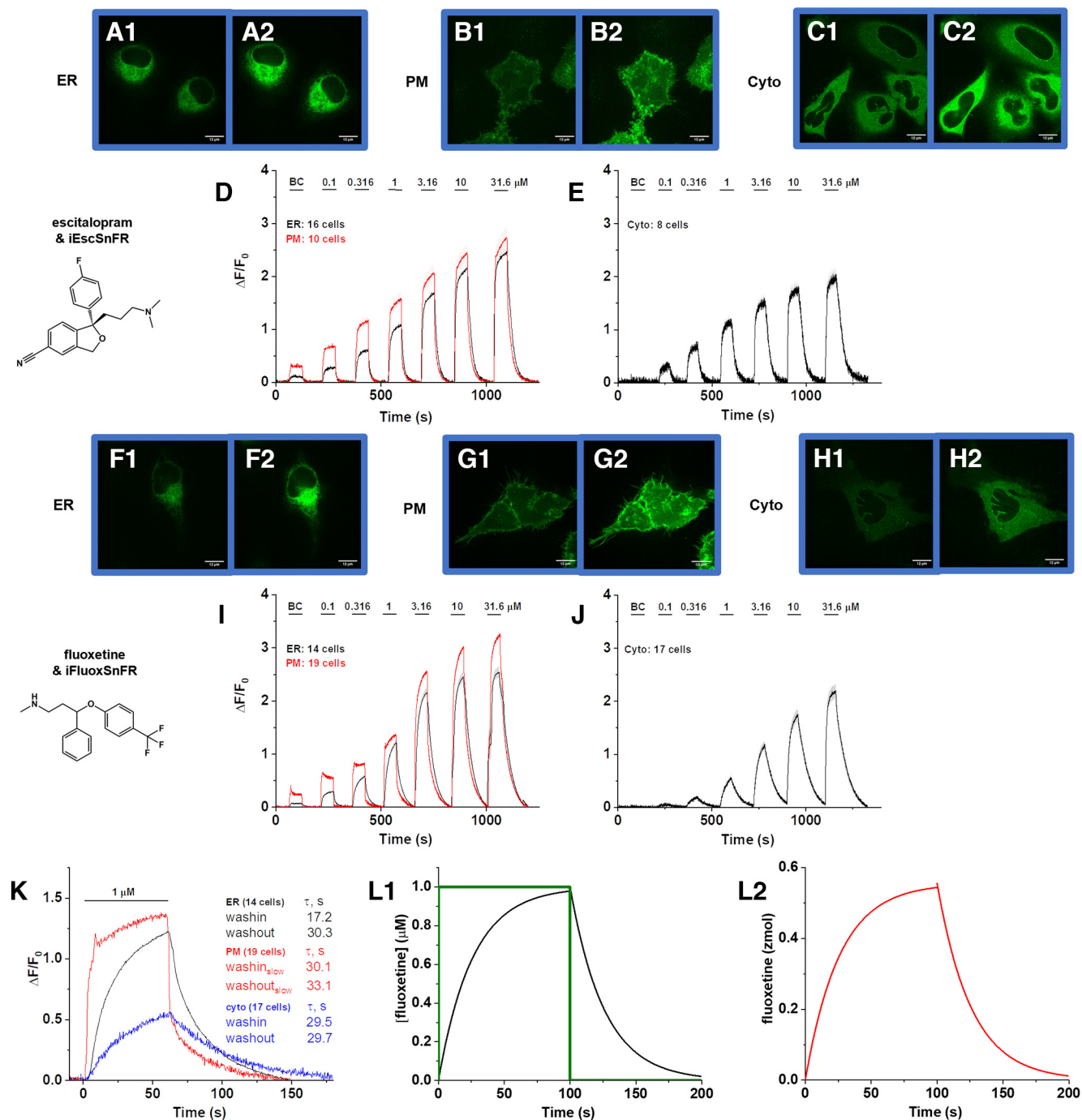


**Figure 7.** Spinning disk laser scanning confocal inverted microscope images of SSRI iDrugSnFRs and ER-, PM-, and cytoplasm-targeted SSRI iDrugSnFR concentration–response relations in HeLa cells. **A1–C2, F1–H2**, ER-targeted constructs of iEscSnFR and iFluoxSnFR are shown before (**A1, F1**) and during (**A2, F2**) exposure to each drug partner at  $10 \mu\text{M}$ . ER-targeted iDrugSnFRs show the eponymous reticulated structure and dark ovals corresponding to the nucleus. PM-targeted constructs of both SSRI iDrugSnFRs are shown before (**B1, G1**) and during (**B2, G2**) exposure to each drug partner at  $10 \mu\text{M}$ . Localization to the PM is robust, with some minimal puncta that may represent inclusion bodies or internal transport. Cytoplasm-targeted constructs of iEscSnFR and iFluoxSnFR are shown before (**C1, H1**) and during (**C2, H2**) exposure to each drug partner at  $10 \mu\text{M}$ . Cytoplasm-targeted iDrugSnFRs show exclusion from the nucleus. **D–E, I–J**, Drugs were applied for 60 s pulses at 90–120 s intervals. Each iDrugSnFR detects its drug partner at the ER, PM, and cytoplasm of HeLa cells at the concentrations sampled. BC, Buffer control. SEM of data are indicated by semitransparent shrouds around traces where trace width is exceeded. **D–E**, iEscSnFR detects escitalopram, approaching a plateau during the application, then returns to baseline fluorescence during the washout, when targeted to the ER, PM, and cytoplasm. **I–J**, iFluoxSnFR targeted to the ER, PM, and cytoplasm detects fluoxetine with a return to baseline fluorescence between applications. **K**, Superimposed waveforms for a 60 s pulse of  $1 \mu\text{M}$  fluoxetine versus iFluoxSnFR targeted to the ER, PM, and cytoplasm in HeLa cells. Tabular values give the time constants  $\tau$  of each phase for ER and cytoplasm as well as  $\tau$  for the slower phase for the PM. **L**, Simulations of the [fluoxetine] within intracellular shells. All intracellular shells superimpose on this time scale. **L1**, The green and black traces are equivalent to their counterparts in Figure 5C except that we have presumed weaker membrane accumulation than in the hippocampal neuron PM. **L2**, Simulated accumulation of fluoxetine within the membrane shell, corresponding to the slower phase of **K** for the PM-localized sensor.

response experiments in primary mouse hippocampal culture (Fig. 4A,C). Of particular note, the kinetic profile of *N,N*-dimethylfluoxetine as detected by iFluoxSnFR\_PM showed a return to baseline fluorescence within seconds after drug washout, a

distinctly different result from the observed profile of fluoxetine as detected by iFluoxSnFR\_PM. iEscSnFR\_ER and iFluoxSnFR\_ER showed little  $\Delta F/F_0$  response to application of their corresponding quaternary derivatives, presumably because the permanent

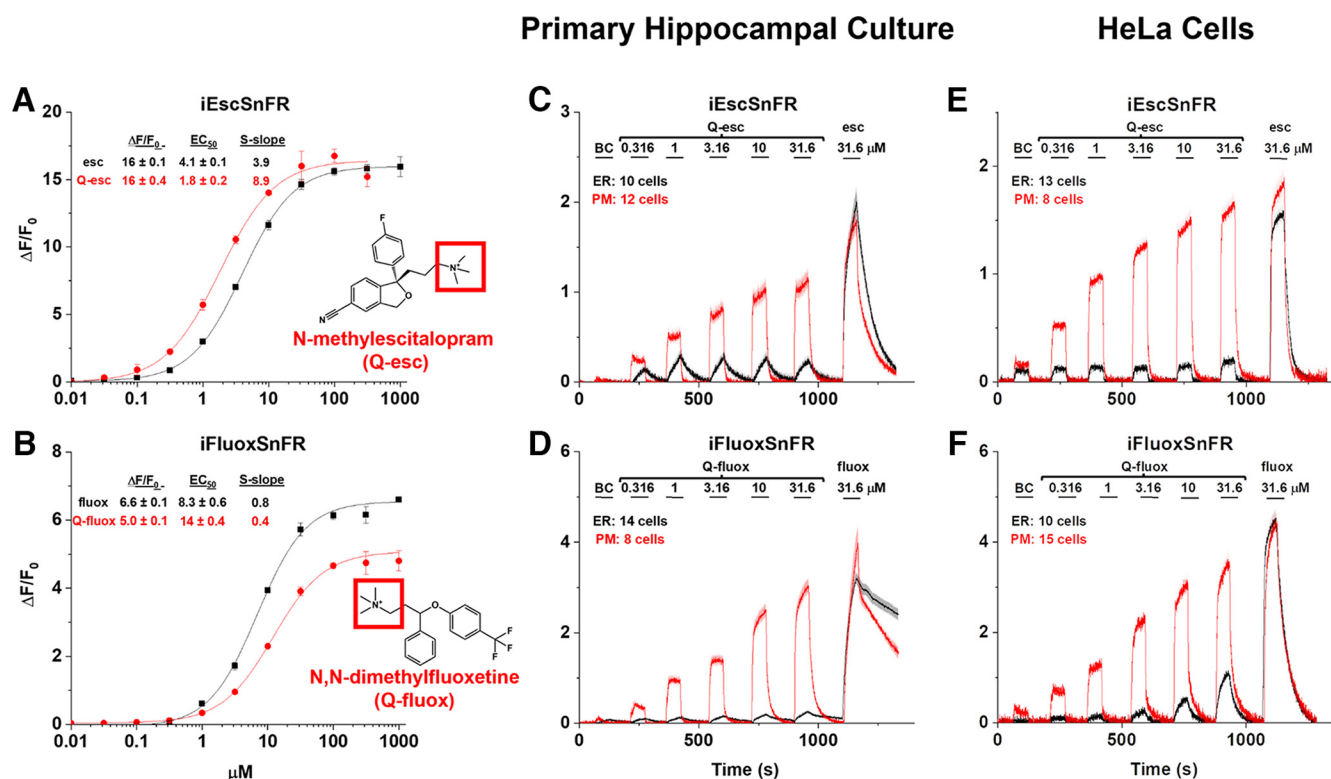


**Figure 8.** Quaternary SSRI derivatives, SSRI iDrugSnFR concentration–response relations in purified protein, primary hippocampal culture, and HeLa cells. **A, B**, *In vitro* concentration–response relations of purified SSRI iDrugSnFRs against quaternary SSRI derivatives. esc, escitalopram; Q-esc, *N*-methylscitalopram; fluox, racemic fluoxetine; Q-fluox, *N,N*-dimethylfluoxetine. iEscSnFR detects *N*-methylscitalopram with an  $EC_{50}$  approximately half that for escitalopram (**A**). iFluoxSnFR detects *N,N*-dimethylfluoxetine with an  $EC_{50}$  approximately twice that for fluoxetine (**B**). **C–F**, Each iDrugSnFR detects its drug partner at the concentrations sampled in primary hippocampal culture and HeLa cells. BC, Buffer control. SEM of data are indicated by semitransparent shrouds around traces where trace width is exceeded. Drugs were applied for 60 s pulses at 90–120 s intervals to cells expressing  $\_ER$  or  $\_PM$  constructs (**C, E**). iEscSnFR $\_PM$  detects the presence of *N*-methylscitalopram, approaching a plateau during application, then returning to baseline during the washout. In contrast, iEscSnFR $\_ER$  is unable to detect *N*-methylscitalopram. A control concentration of escitalopram (final application) is detected by both the  $\_PM$ - and  $\_ER$ -targeted constructs (**C, E**). **D, F**, iFluoxSnFR $\_PM$  detects *N,N*-dimethylfluoxetine with a near approach to a plateau during each application, and with a return to baseline during the washout. In contrast, iFluoxSnFR $\_ER$  in primary hippocampal culture does not detect *N,N*-dimethylfluoxetine, and iFluoxSnFR $\_ER$  in HeLa cells detects *N,N*-dimethylfluoxetine above BC only at concentrations above  $10 \mu M$ . A control concentration of fluoxetine is detected by both the  $\_PM$ - and  $\_ER$ -targeted constructs (final application). Application of fluoxetine in primary hippocampal culture reproduces the slowly increasing rising phase and the extended washout observed in Figure 4 **C, D**.

positive charges on the quaternary drugs result in a reduced ability to cross membranes.

We also performed concentration–response experiments with the quaternary SSRIs in HeLa cells transfected with  $\_PM$ - and  $\_ER$ -targeted constructs of iEscSnFR and iFluoxSnFR (Fig. 8*E, F*). The  $\_PM$ -targeted constructs detected their respective quaternary SSRI derivatives over the  $0.1$ – $31.6 \mu M$  range sampled, with characteristics similar to those detected in primary hippocampal culture (Fig. 8*C, D*). The detection of quaternary SSRI by the  $\_ER$ -targeted constructs was likewise minimal, with the exception that iFluoxSnFR $\_ER$  had  $\Delta F/F_0$  above baseline for *N,N*-dimethylfluoxetine at concentrations above  $3.16 \mu M$ . The iFluoxSnFR $\_ER$  signal above baseline stays below  $\sim 20\%$  of the fluorescence signal of the  $\_PM$  construct and represents concentrations above clinical relevance.

To examine the limits of membrane impermeability for quaternary SSRI derivatives, we tested an extended period of coinubation (Fig. 9). We transfected the  $\_ER$  and  $\_PM$  constructs of both iEscSnFR and iFluoxSnFR into HeLa cells and incubated these cells with  $500 \text{ nM}$  drug (a concentration with appreciable  $\Delta F/F_0$  and within a log unit of the physiologically relevant concentrations of escitalopram and fluoxetine *in vivo*; Karson et al., 1992; Renshaw et al., 1992; Bolo et al., 2000; Paulzen et al., 2016). We incubated transfected HeLa cells with either an SSRI or a quaternary derivative for 2.4 h (Fig. 9). After transfer to the

imaging rig and an equilibration period with buffer containing an identical concentration of the incubation drug, we started a program that included a buffer wash, a short introduction of the complementary compound (i.e., quaternary SSRI if the incubation drug was an SSRI or vice versa), a second buffer wash, and finally a reintroduction of the incubation compound (Fig. 9).

When SSRIs were preincubated with  $\_ER$  constructs, we saw an initial fluorescence signal that indicated that the SSRIs were present in the ER. Application of buffer decreased the fluorescence signal to a new baseline. Subsequent application of the quaternary SSRIs caused no appreciable increase in fluorescence signal, presumably because the quaternary SSRIs were unable to cross into the ER. A reapplication of the SSRIs also provided biosensor fluorescence signal over background in the ER, although the  $\Delta F/F_0$  of the reapplication is  $\sim 50\%$  of the signal observed after the 2.4 h incubation. Possibly the  $\Delta F/F_0$  would have returned to its maximum value if the reapplication occurred over a longer period (Fig. 9, first row).

When the SSRIs were preincubated with cells expressing the  $\_PM$  construct, introduction of control HBSS (Fig. 9, second row) produced a decrease to a new baseline. As would be predicted, in this case, reapplication of quaternary SSRIs generated a reversible fluorescence increase because  $\_PM$ -targeted biosensor was accessible to detect the quaternary drug. Reapplication of the SSRIs once again generated a fluorescence signal over baseline,

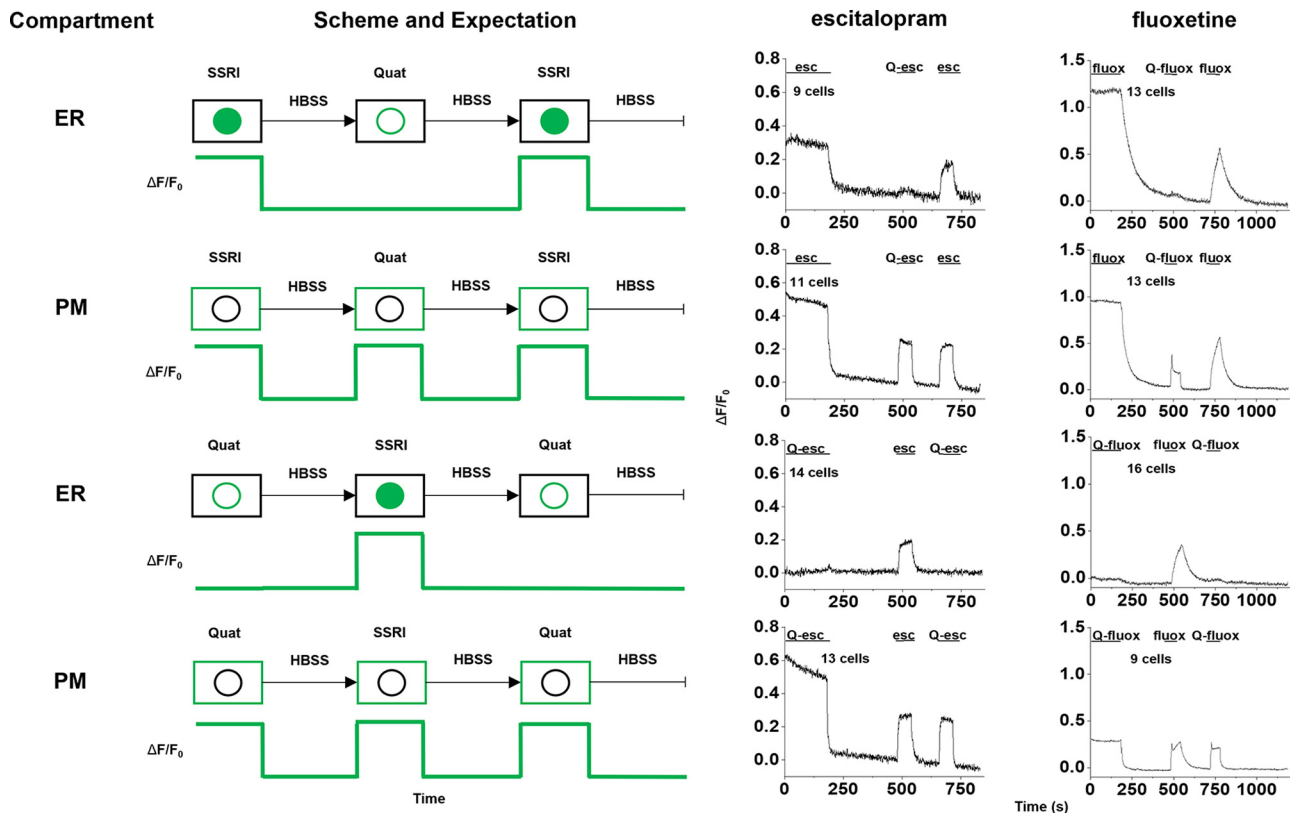


**Figure 9.** A 2.4 h incubation of SSRIs and quaternary derivatives with HeLa cells. esc, escitalopram; Q-esc, *N*-methylescitalopram; fluox, racemic fluoxetine; Q-fluox, *N,N*-dimethylfluoxetine. Left column, Targeted compartment of the SSRI biosensor. Middle column, Scheme and expectation of fluorescence response by biosensor based on compartment targeted and preincubated drug. Following preincubation, the drug is washed out, after which the alternate drug is washed in (i.e., when SSRI was preincubated, the quaternary derivative (labeled Quat) was applied and vice versa). An additional washout follows; then the originally preincubated drug is reapplied. Right columns, Fluorescence response of escitalopram and fluoxetine by their corresponding iDrugSnFR after preincubation, washes, and subsequent drug applications, agreeing with the expectations described for the middle column.

although this signal was again  $\sim 50\%$  of the signal inferred from the end of the 2.4 h incubation (Fig. 9, second row).

When quaternary SSRIs were preincubated with ER-targeted biosensors, introduction of control HBSS (Fig. 9, third row) did not produce a clear decrease in biosensor fluorescence signal. Rather, the signal we observed continued as the existing baseline, with little to no change in signal. Upon application of SSRI, we observed a clear reversible increase in  $\Delta F/F_0$  over the baseline fluorescence signal in the ER, which indicated that SSRIs could reach the ER freely. Reapplication of the quaternary SSRI did not generate an increase in biosensor fluorescence signal over the existing baseline, which indicated that the quaternary compound still did not cross into the ER (Fig. 9, third row). Incubation of quaternary SSRIs with the PM-targeted biosensors (Fig. 9, fourth row) resembled the signals obtained after the 2.4 h incubation of the SSRIs with the PM-targeted biosensors (Fig. 9, second row).

When we attempted a 24 h preincubation with drug, we experienced a low  $\Delta F/F_0$  that was confounded by high background (data not shown). We abandoned experiments with the 24 h preincubation.

#### Membrane-impermeant SSRI derivatives are modestly weaker SERT blockers

The membrane-impermeant quaternary SSRI derivatives provided an opportunity to test the hypothesis that the potency of SSRIs at SERT arises, in part, because they approach their binding site from the membrane phase. To compare the results with the time scale of our fluorescence experiments, we used temporally resolved measurements on the transport-related current

evoked by 5-HT (Mager et al., 1994), using an hSERT mutant that has unusually large transport-associated currents at low pH (Cao et al., 1997).

With membrane-bound hSERT in living cells, we found that *N,N*-dimethylfluoxetine blocks hSERT with an  $IC_{50} \sim 12$ -fold higher than fluoxetine (Fig. 10A,C). With membrane-bound hSERT in living cells, we found that *N*-methylescitalopram blocks hSERT with an  $IC_{50}$  about sixfold greater than escitalopram (Fig. 10B,D). In more conventional experiments using [ $^3$ H]serotonin flux, quaternary citalopram blocked hSERT with a 10-fold higher  $IC_{50}$  than citalopram (Bismuth-Evenzal et al., 2010). These modest differences between the SSRIs and their quaternary derivatives do not strongly support the hypothesis that fluoxetine and escitalopram approach their binding site from the membrane (see below, Discussion).

#### Intracellularly bioavailable fluoxetine and escitalopram equal the extracellular values but represent a small fraction of the total cellular drug because of lipid binding

To complement the iDrugSnFR experiments, we performed a series of measurements to measure both the ratio between the concentration of intracellular unbound (bioavailable) compound and that of the external solution ( $F_{ic}$ ), and the total cellular drug accumulation ratio ( $K_p$ ). We used cultured HEK293 cells, which provide a rough approximation (within twofold) to brain binding (Mateus et al., 2014).

We first describe the  $K_p$  data.  $K_p$  did not fully reach equilibrium for fluoxetine and escitalopram, with a peak at 30 min and

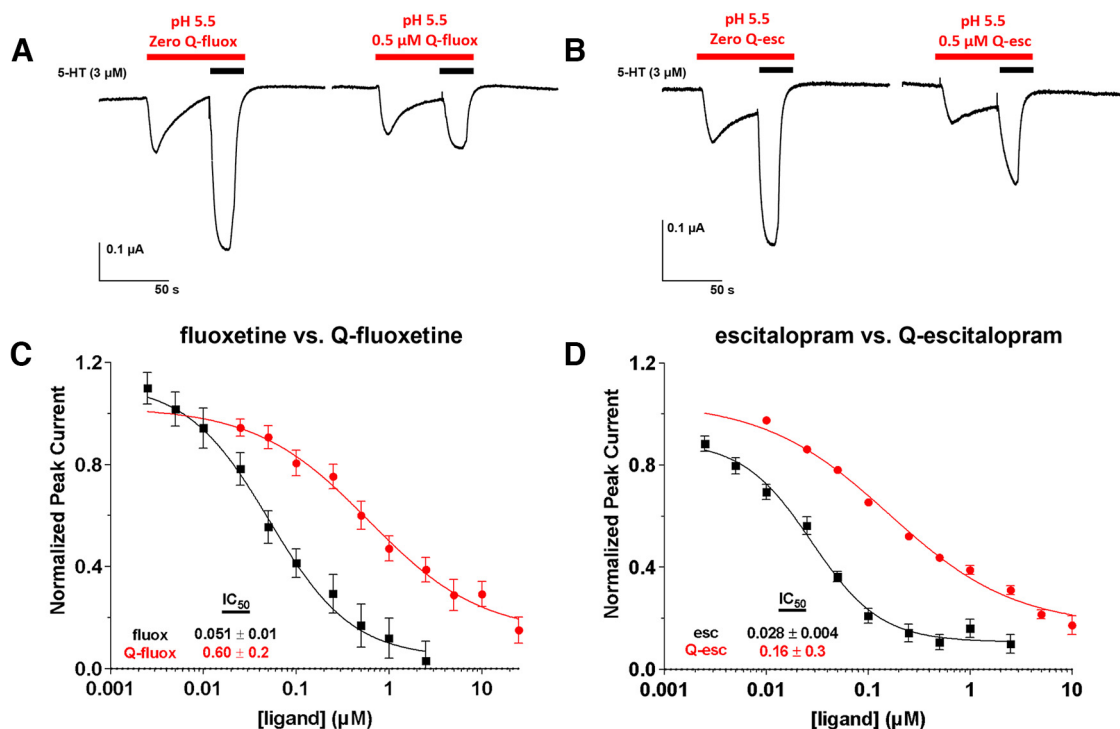


**Figure 10.** Inhibition of 5-HT-induced hSERT transport-associated currents by SSRIs and their quaternary derivatives. esc, escitalopram; Q-esc, *N*-methylescitalopram; fluox, racemic fluoxetine; Q-fluox, *N,N*-dimethylfluoxetine. **A, B**, Exemplar traces of 5-HT-induced hSERT currents in the absence and presence of Q-fluox and Q-esc respectively. **C, D**, Inhibition of 5-HT-induced hSERT currents of fluoxetine vs. *N,N*-dimethylfluoxetine and escitalopram vs. *N*-methylescitalopram, respectively.  $IC_{50}$  values and Hill coefficients, calculated from the corresponding fit. *N,N*-dimethylfluoxetine ( $n = 11$ ) had an  $IC_{50}$  12-fold higher than fluoxetine ( $n = 13$ ) for the inhibition of hSERT transport-associated currents (**C**). *N*-methylescitalopram ( $n = 24$ ) had an  $IC_{50}$  sixfold higher than escitalopram ( $n = 18$ ) for the inhibition of hSERT transport-associated currents (**D**).

a subsequent decrease during the period leading up to 120 min. At 30 and 120 min,  $K_p = 1590 \pm 150$ , and  $1170 \pm 50$ , respectively (geometric mean  $\pm$  SEM). The escitalopram  $K_p$  values were 12-fold smaller at 30 and 120 min,  $132 \pm 12$  and  $67 \pm 30$  (geometric mean  $\pm$  SEM). The values for  $K_p$  (Fig. 11A) are among the largest measured for any drug (Treyer et al., 2018).

Recent experiments show that the intracellular unbound fraction of drug ( $f_{u,cell}$ ) is dominated by distribution into cellular membrane phospholipids (Treyer et al., 2018, 2019). We determined  $f_{u,cell}$  for HEK293 cells with lipid membrane-coated beads using the approach developed by Treyer et al. (2019). The phosphatidylcholine coating substitutes approximately for measurements with phospholipid mixtures from individual cell types (Treyer et al., 2019), which were unavailable for these experiments. The experiments use a 12 min incubation, a time scale relevant to the iDrugSnFR experiments. The  $f_{u,cell}$  was 0.0006 for fluoxetine and 0.0085 for escitalopram. Thus, most of the intracellular drug is bound to lipids, and escitalopram binds less strongly than fluoxetine, consistent with the idea that iDrugSnFR kinetics for escitalopram were  $\sim 10$ -fold faster than fluoxetine kinetics (Figs. 4, 7) because diffusion of escitalopram through the membrane is buffered less by binding within the membrane.

The  $K_p$  and  $f_{u,cell}$  data then determined  $F_{ic}$  (Fig. 11B).  $F_{ic}$  ranged between 0.5 and 1.0 for both fluoxetine and escitalopram, after 60 minutes. This dataset was presumably dominated by cytoplasmically located drug, because the ER accounts for just  $\sim 10\%$  of total intracellular volume, and other organelles represent even smaller volumes. The dataset thus agrees well with the similar  $\Delta F/F_0$  measurements for the  $_{cyto}$  iDrugSnFRs versus free solution values. Because  $F_{ic}$  is proportional to  $K_p$ ,  $F_{ic}$  decreases by  $\sim 40$ – $50\%$  between 60 min and 120 min. We have not systematically studied the origin of the decline,

which was not observed for the two control drugs, atorvastatin and lopinavir.

The Discussion (see below) raises the possibility that unusual kinetic properties of fluoxetine in neurons arise from membrane cholesterol. Unfortunately, the bead manufacturer does not supply beads with known or calibrated cholesterol content. Therefore, it is not yet possible to perform systematic experiments on this point.

In summary, chemical determination shows that applied fluoxetine or escitalopram enters the cell within 30 min. Of the intracellular SSRI,  $>99\%$  is bound to lipids and is therefore available for interaction with membrane proteins. Although  $<1\%$  of intracellular fluoxetine or escitalopram is unbound, this concentration roughly equals that of the external solution and is also available for interaction with SERT or other molecules.

## Discussion

### Two SSRIs enter several cellular compartments

The present data establish that fluoxetine and escitalopram, two commonly used hSERT ligands, enter both the cytoplasm and the ER (the largest organelle) within at most a few minutes after the drugs appear outside a neuron (Fig. 4) or a HeLa cell (Fig. 7). The drugs leave with a similar time course after the extracellular [drug] is stepped to zero. That fluoxetine and escitalopram appear as unbound molecules at concentrations near the extracellular values is confirmed by chemical detection within HEK293 cells, a good model for intracellular pharmacokinetics of neurons (Mateus et al., 2013), albeit with less precise temporal resolution (Fig. 11).

At the same time the drugs are equilibrating with the cytoplasm and ER, the drugs are accumulating within the PM (Figs.

5, 8, 11) and, presumably, the other membranes. We inferred the quantitative extent of accumulation within the membrane from iDrugSnFR waveforms. For fluoxetine sensed by iFluoxSnFR, our data for neurons and HeLa cells are consistent with concentration ratios of 180 (Fig. 5) and 18 (Fig. 7), respectively. The predicted  $\text{LogD}_{\text{pH}7.4}$  value for fluoxetine corresponds to a concentration ratio of 67, but octanol and plasma membrane probably have different matrix properties. For pure phosphatidylcholine membranes on beads (this study), or for ITC measurement on pure 1,2-dierucoyl-*sn*-glycero-3-phosphocholine (Kapoor et al., 2019), the fluoxetine accumulation ratio is 30–300 times higher than we infer from iFluoxSnFR waveforms at the PM.

The data provide only slight support for the idea that both fluoxetine and escitalopram interact with SERT more strongly when approaching from the membrane than from an aqueous phase. The potency of membrane-impermeant quaternary derivatives as hSERT blockers is modestly (sixfold to 10-fold) less than the potency of the SSRIs themselves (Fig. 10).

### Contributions of SSRI iDrugSnFRs to the iDrugSnFR paradigm

This study expands the iDrugSnFR family of sensors (Bera et al., 2019; Shivange et al., 2019; Muthusamy et al., 2022; Nichols et al., 2022) to include SSRIs. SSRI iDrugSnFRs are sensitive enough to allow experiments near the experimentally determined (or otherwise projected) concentration in human blood and CSF (Karson et al., 1992; Renshaw et al., 1992; Bolo et al., 2000; Paulzen et al., 2016).

Our previous applications of iDrugSnFRs have used such sensors to measure the free aqueous concentration of a drug. The present experiments show that at least one iDrugSnFR, iFluoxSnFR, can also detect fluoxetine in the membrane that anchors the iDrugSnFR. The iDrugSnFR experiments are well suited to the apparent time scale of accumulation. This additional, useful feature presumably arises because the fluoxetine accumulates (our iDrugSnFR data are best fitted by a factor  $\sim 181$ ) in the membrane just a few angstroms from the binding site of iDrugSnFR. Similar accumulation in lipids also underlies the high volume of distribution ( $\sim 20$  L/kg) that generally characterizes SSRIs and tricyclic antidepressants. Other major antidepressant classes (serotonin-norepinephrine reuptake inhibitors and S-ketamine) have much lower volumes of distribution.

Some conventional measurements on SSRIs employ intracerebral microdialysis, with 10–20 min sampling intervals (Fukushima et al., 2004; Bundgaard et al., 2007b; O'Brien et al., 2013) to examine 5-HT (or other neurotransmitter) levels (Cryan et al., 2004; Bundgaard et al., 2007a; Deltheil et al., 2009; Gardier, 2013). Neurotransmitter levels serve as an indirect indicator of SSRI concentration. Thus, imaging- or photometry-based examination of the local brain concentrations of local, free (unbound) antidepressant in real-time using iDrugSnFRs could provide valuable information on SSRI pharmacokinetics.

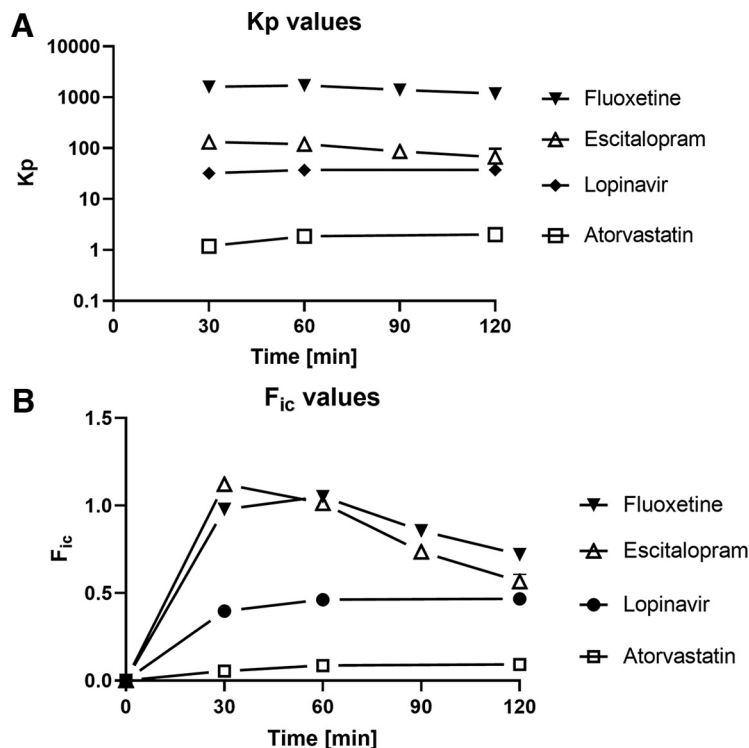


**Figure 11.** SSRIs are highly bioavailable intracellularly despite substantial membrane binding. **A**,  $K_p$  values, measuring total cellular accumulation in living HEK293 cells at 30–120 min of incubation. **B**,  $F_{ic}$  values measuring the ratio between unbound intracellular (mostly cytoplasmic) concentration and the external solution. SEM values are shown where they exceed the size of data markers.

### Fluoxetine versus escitalopram

Our study exploited an important feature of a reduced cellular model; we performed experiments in parallel on two therapeutic agents thought to act similarly. The iDrugSnFRs themselves differ by only eight amino acids near the PBP binding site and two near the PBP-cpGFP linkers (four differences are shown in Fig. 1A, and full sequences are given in the Addgene deposits. See Materials and Methods, Plasmid availability). The drugs themselves have rather similar  $\text{LogD}_{\text{pH}7.4}$  and  $\text{pK}_a$  values. We reasoned that any property governing SSRIs as a class would result in similar measurements for fluoxetine and escitalopram. We found two classes of shared properties: entry into the cytoplasm and ER, and accumulation in membranes.

Nonetheless, it is important to understand the different properties of fluoxetine and escitalopram. In medical practice, escitalopram produces fewer adverse events than fluoxetine (Kennedy et al., 2009), and fluoxetine results in a less frequent and less severe antidepressant discontinuation syndrome (Fava et al., 2015). All the present datasets are consistent with previous data that escitalopram accumulates in membranes or lipids roughly an order of magnitude less than fluoxetine (Wan et al., 2007; Lanevskij et al., 2011; Mateus et al., 2014; Kapoor et al., 2019). In the diffusion-bonding model, this difference explains how escitalopram enters and leaves the compartments we studied at least an order of magnitude faster than fluoxetine. The  $\text{LogP}$  and  $\text{LogD}_{\text{pH}7.4}$  for escitalopram are  $\sim 0.5$  less than for fluoxetine, perhaps corresponding to part of the difference in accumulation. The difference between fluoxetine and escitalopram is unlikely to arise from drug efflux pumps (Peters et al., 2009) but could arise from one or more other mechanisms, including kinetics of partitioning into lipid rafts (Senese and Rasenick, 2021), lateral diffusion

within the plane of the membrane, and effects on membrane elasticity and curvature (Kapoor et al., 2019).

### Cultured neurons versus HeLa cells

We conclude that fluoxetine (and probably escitalopram) accumulates in membranes of cultured neurons ~10-fold more strongly than in membranes of HeLa cells (Figs. 5C1,C2, 7L1,L2). Possibly the differences arise from the presence of the glial layer in the primary neuron cultures. Glia furnish most of the cholesterol in neuronal membranes (Pfrieger and Ungerer, 2011). SSRIs interact directly with cholesterol-rich membranes (Erb et al., 2016), changing their structure (Momo et al., 2005); SSRIs change cholesterol levels in the brain and SSRIs help TRKB to sense cholesterol (Casarotto et al., 2021). Temporal and causal relations among these phenomena are not yet understood. Therefore, it will be of interest to determine whether astrocyte-supplied cholesterol underlies our observation that fluoxetine interacts for several hundred seconds with neuronal membranes.

### Insights from quaternary SSRI derivatives

Use of impermeant quaternary blocking drugs is an accepted paradigm in ion channel and receptor pharmacology (Hille, 1977a,b; Shivange et al., 2019), and we performed analogous experiments with a neurotransmitter transporter. Some data suggest that fluoxetine stabilizes SERT in a conformation that exposes the binding site to the internal solution (Tavoulari et al., 2009), but atomic-scale structures suggest that bound escitalopram faces the external solution (Coleman et al., 2016). Neither of the two cited studies addresses the question of whether the SSRI approaches the binding site from the membrane or from the aqueous phase.

On the one hand, the modest decreases in affinity for the impermeant derivatives (sixfold to 12-fold) provide little support for the membrane approach mechanism. The protonated amine of several SSRIs makes a cation- $\pi$  interaction with Tyr95 and a hydrogen bond with Asp98 of SERT (Coleman and Gouaux, 2018). Quaternization of the amine would alter the former interaction and eliminate the latter, possibly decreasing the affinity by the observed amounts. On the other hand, the impermeant derivatives will provide a convenient probe to distinguish effects of SERT blockade from intracellular effects of SSRI-SERT interactions, for at least 2.4 h (Fig. 9).

Fluoxetine binds to TRKB in the deprotonated form (Casarotto et al., 2021), vitiating any conclusions about membrane approach from measurements on quaternary SSRI derivatives at TRKB. Therefore, we did not perform experiments on the interaction between the quaternary SSRI derivatives and TRKB.

### Implications for the four possible mechanisms of SSRI action

Returning to the four nonexclusive mechanisms summarized in the Introduction, Mechanism (1), the outside-in mechanism, is not informed by our data. Outside-in processes operate via SSRI-driven changes in external 5-HT concentration, which we did not study.

Mechanism (2), the hypothesis that SSRI levels during the therapeutic lag are governed by whole-animal or organ-level pharmacokinetic properties, is not supported by our experiments—even if one assumes that myelin, with some 500 membranes in parallel, increases the wash-in and washout time constants for fluoxetine (300 s) by 500-fold. This would extend the times to  $1.5 \times 10^4$  s, or 1 d, enough to explain the classically measured disappearance of fluoxetine but still ~10-fold less than the therapeutic lag. If, in the future, experiments

on myelin show that the slowing of diffusion varies quadratically rather than linearly with the number of membrane layers, then membrane accumulation might explain how ~21 d of fluoxetine treatment are required before fluoxetine is detectable in humans via *in vivo* nuclear magnetic resonance spectroscopy (Karson et al., 1992). The faster kinetics for escitalopram further undercut the idea that lipid accumulation can explain the therapeutic lag for SSRIs. However, use of SSRIs in premenstrual syndrome is apparently not associated with a therapeutic lag (Steinberg et al., 2012). The time course of antidepressant discontinuation syndrome is also relatively rapid compared with the classical therapeutic lag. Therefore, the purely pharmacokinetic hypothesis is being investigated further (Senese and Rasenick, 2021).

Mechanism (3), the hypothesis that therapeutic effects occur at least partially because of SSRI-SERT interactions in cellular compartments other than the extracellular-facing surface of the PM, is consistent with our observations. Given the dimerization and quality control processes that transporters undergo in the ER, target engagement within the ER, including pharmacological chaperoning of nascent SERT, continues as a suspected therapeutic mechanism (Lester et al., 2012). That fluoxetine enters the ER may also explain how fluoxetine induces cytotoxic ER stress (Bowie et al., 2015). The vast SSRI accumulation within membranes and the decreased potency of membrane-excluded derivatives raises the possibility that SSRI-SERT engagement is enhanced because it occurs within the PM or an organellar membrane—a suggestion that broadens the meaning of the earlier phrase, “inside-out” (Lester et al., 2012).

Presently available iDrugSnFRs cannot function in acidic organelles; therefore, the indirect, relatively insensitive experiments on acid trapping in acidic organelles were uninformative (Fig. 6). Because endolysosomal compartments account for ~1% of the total volume of a cell (Mateus et al., 2013), even the predicted ~100-fold accumulation (Fig. 6A) because of acid trapping would produce an overall fluoxetine accumulation of just about twofold, or several orders of magnitude lower than the directly measured  $K_p$  because of membrane accumulation of fluoxetine (Fig. 11). Furthermore, acid trapping would reach completion within a few hundred seconds, too slow to explain the therapeutic lag. When acid-tolerant iDrugSnFRs are eventually developed, it may become possible to directly examine another hypothesis: endosome-based SERT recycling (Riad et al., 2001, 2004).

In Mechanism (4), additional pathways are consistent with our experiments to the extent that they involve SSRIs within membranes, especially neuronal membranes. Such pathways include interactions with TRKB (Casarotto et al., 2021), lipid rafts (Senese and Rasenick, 2021), or lipid-modifying enzymes (Kornhuber and Gulbins, 2021).

The hSERT ligands studied here have important continuing uses in medicine. These uses call for further investigations into the neuroscientific basis of their action(s).

### References

- Alberts B, Bray D, Lewis J, Morgan D, Raff M, Roberts K, Walter P, Wilson J, Hunt TW (2015) Molecular biology of the cell. New York: Garland Science.
- Armstrong D, Lester HA (1979) The kinetics of tubocurarine action and restricted diffusion within the synaptic cleft. *J Physiol* 294:365–386.
- Baldwin DS (2002) Escitalopram: efficacy and tolerability in the treatment of depression. *Hosp Med* 63:668–671.
- Beasley CM Jr, Nilsson ME, Koke SC, Gonzales JS (2000) Efficacy, adverse events, and treatment discontinuations in fluoxetine clinical studies of

- major depression: a meta-analysis of the 20-mg/day dose. *J Clin Psychiatry* 61:722–728.
- Beatty Z, Muthusamy A, unger E, Dougherty DA, Tian L, Looger LL, Shivange AV, Bera K, Lester HA, Nichols A (2022) Fluorescence screens for identifying central nervous system-acting drug-biosensor pairs for subcellular and supracellular pharmacokinetics. *Bio Protoc* 12:e4551.
- Belmaker RH, Agam G (2008) Major depressive disorder. *N Engl J Med* 358:55–68.
- Bera K, Kamajaya A, Shivange AV, Muthusamy AK, Nichols AL, Borden PM, Grant S, Jeon J, Lin E, Bishara I, Chin TM, Cohen BN, Kim CH, Unger EK, Tian L, Marvin JS, Looger LL, Lester HA (2019) Biosensors show the pharmacokinetics of S-ketamine in the endoplasmic reticulum. *Front Cell Neurosci* 13:499.
- Bismuth-Evenzal Y, Roz N, Gurwitz D, Rehavi M (2010) N-methyl-citalopram: a quaternary selective serotonin reuptake inhibitor. *Biochem Pharmacol* 80:1546–1552.
- Bolo NR, Hodé Y, Nédélec JF, Lainé E, Wagner G, Macher JP (2000) Brain pharmacokinetics and tissue distribution *in vivo* of fluvoxamine and fluoxetine by fluorine magnetic resonance spectroscopy. *Neuropsychopharmacology* 23:428–438.
- Borden P, Shivange AV, Marvin JS, Cichon J, Dan C, Podgorski K, Novak O, Tanimoto M, Lobas M, Khakh B, Dittman J, Gan W, Koyama M, Jayaraman V, Zhu J, Lester HA, Looger LL (2019) A genetically encoded fluorescent sensor for *in vivo* acetylcholine detection. *Nat Biotechnol* 6:726–737.
- Bowie M, Pilie P, Wulffkuhle J, Lem S, Hoffman A, Desai S, Petricoin E, Carter A, Ambrose A, Seewaldt V, Yu D, Ibarra Drendall C (2015) Fluoxetine induces cytotoxic endoplasmic reticulum stress and autophagy in triple negative breast cancer. *World J Clin Oncol* 6:299–311.
- Bundgaard C, Jørgensen M, Mørk A (2007a) An integrated microdialysis rat model for multiple pharmacokinetic/pharmacodynamic investigations of serotonergic agents. *J Pharmacol Toxicol Methods* 55:214–223.
- Bundgaard C, Jørgensen M, Larsen F (2007b) Pharmacokinetic modelling of blood–brain barrier transport of escitalopram in rats. *Biopharm Drug Dispos* 28:349–360.
- Burke WJ, Gergel I, Bose A (2002) Fixed-dose trial of the single isomer SSRI escitalopram in depressed outpatients. *J Clin Psychiatry* 63:331–336.
- Cao Y, Mager S, Lester HA (1997) H<sup>+</sup> permeation and pH regulation at a mammalian serotonin transporter. *J Neurosci* 17:2257–2266.
- Casarotto PC, et al. (2021) Antidepressant drugs act by directly binding to TRKB neurotrophin receptors. *Cell* 184:1299–1313.e19.
- Challis RC, Kumar SR, Chan KY, Challis C, Beadle K, Jang MJ, Kim HM, Rajendran PS, Tompkins JD, Shivkumar K, Deverman BE, Gradinaru V (2019) Publisher correction: systemic AAV vectors for widespread and targeted gene delivery in rodents. *Nat Protoc* 14:2597.
- Clevenger SS, Malhotra D, Dang J, Vanle B, IsHak WW (2018) The role of selective serotonin reuptake inhibitors in preventing relapse of major depressive disorder. *Ther Adv Psychopharmacol* 8:49–58.
- Coleman JA, Gouaux E (2018) Structural basis for recognition of diverse antidepressants by the human serotonin transporter. *Nat Struct Mol Biol* 25:170–175.
- Coleman JA, Green EM, Gouaux E (2016) X-ray structures and mechanism of the human serotonin transporter. *Nature* 532:334–339.
- Crank J (1975) *The mathematics of diffusion*. Oxford, UK: Clarendon Press.
- Cryan JF, O’Leary OF, Jin SH, Friedland JC, Ouyang M, Hirsch BR, Page ME, Dalvi A, Thomas SA, Lucki I (2004) Norepinephrine-deficient mice lack responses to antidepressant drugs, including selective serotonin reuptake inhibitors. *Proc Natl Acad Sci U S A* 101:8186–8191.
- Deltheil T, Tanaka K, Repérant C, Hen R, David DJ, Gardier AM (2009) Synergistic neurochemical and behavioural effects of acute intrahippocampal injection of brain-derived neurotrophic factor and antidepressants in adult mice. *Int J Neuropsychopharmacol* 12:905–915.
- Erb SJ, Schappi JM, Rasenick MM (2016) Antidepressants accumulate in lipid rafts independent of monoamine transporters to modulate redistribution of the G protein, *Gas*. *J Biol Chem* 291:19725–19733.
- Fava GA, Gatti A, Belaise C, Guidi J, Offidani E (2015) Withdrawal symptoms after selective serotonin reuptake inhibitor discontinuation: a systematic review. *Psychother Psychosom* 84:72–81.
- Fukushima T, Naka-aki E, Guo X, Li F, Vankeirsbilck V, Baeyens WRG, Imai K, Toshimasa T (2004) Determination of fluoxetine and norfluoxetine in rat brain microdialysis samples following intraperitoneal fluoxetine administration. *Analytica Chimica Acta* 522:99–104.
- Gardier AM (2013) Antidepressant activity: contribution of brain microdialysis in knock-out mice to the understanding of BDNF/5-HT transporter/5-HT autoreceptor interactions. *Front Pharmacol* 4:98.
- Gibson DG, Young L, Chuang RY, Venter JC, Hutchison CA 3rd, Smith HO (2009) Enzymatic assembly of DNA molecules up to several hundred kilobases. *Nat Methods* 6:343–345.
- Govind AP, Vallejo YF, Stolz JR, Yan JZ, Swanson GT, Green WN (2017) Selective and regulated trapping of nicotinic receptor weak base ligands and relevance to smoking cessation. *Elife* 6:e25651.
- Güttler T, Madl T, Neumann P, Deichsel D, Corsini L, Monecke T, Ficner R, Sattler M, Görlich D (2010) NES consensus redefined by structures of PKI-type and Rev-type nuclear export signals bound to CRM1. *Nat Struct Mol Biol* 17:1367–1376.
- Hille B (1977a) The pH-dependent rate of action of local anesthetics on the node of Ranvier. *J Gen Physiol* 69:475–496.
- Hille B (1977b) Local anesthetics: hydrophilic and hydrophobic pathways for the drug-receptor reaction. *J Gen Physiol* 69:497–515.
- Kapoor R, Peyear TA, Koeppe RE, 2nd, Andersen OS (2019) Antidepressants are modifiers of lipid bilayer properties. *J Gen Physiol* 151:342–356.
- Karson CN, Newton JE, Mohanakrishnan P, Sprigg J, Komoroski RA (1992) Fluoxetine and trifluoperazine in human brain: a 19F-nuclear magnetic resonance spectroscopy study. *Psychiatry Res* 45:95–104.
- Kennedy SH, Andersen HF, Thase ME (2009) Escitalopram in the treatment of major depressive disorder: a meta-analysis. *Curr Med Res Opin* 25:161–175.
- Kille S, Acevedo-Rocha CG, Parra LP, Zhang ZG, Opperman DJ, Reetz MT, Acevedo JP (2013) Reducing codon redundancy and screening effort of combinatorial protein libraries created by saturation mutagenesis. *ACS Synth Biol* 2:83–92.
- Kornhuber J, Gullbins E (2021) New molecular targets for antidepressant drugs. *Pharmaceuticals (Basel)* 14:894.
- Lalit V, Appaya PM, Hegde RP, Mital AK, Mittal S, Nagpal R, Palaniappan V, Ramsbramaniam C, Rao GP, Roy K, Trivedi JK, Vankar GK, Karan RS, Shah S, Patel RB (2004) Escitalopram versus citalopram and sertraline: a double-blind controlled, multi-centric trial in Indian patients with unipolar major depression. *Indian J Psychiatry* 46:333–341.
- Lanevskij K, Dapkunas J, Juska L, Japertas P, Didziapetris R (2011) QSAR analysis of blood–brain distribution: the influence of plasma and brain tissue binding. *J Pharm Sci* 100:2147–2160.
- Lee-Kelland R, Zehra S, Mappa P (2018) Fluoxetine overdose in a teenager resulting in serotonin syndrome, seizure and delayed onset rhabdomyolysis. *BMJ Case Rep* 2018:bcr2018225529.
- Lepola UM, Loft H, Reines EH (2003) Escitalopram (10–20 mg/day) is effective and well tolerated in a placebo-controlled study in depression in primary care. *Int Clin Psychopharmacol* 18:211–217.
- Lester HA, Xiao C, Srinivasan R, Son C, Miwa J, Pantoja R, Dougherty DA, Banghart MR, Goate AM, Wang JC (2009) Nicotine is a selective pharmacological chaperone of acetylcholine receptor number and stoichiometry. implications for drug discovery. *AAPS J* 11:167–177.
- Lester HA, Miwa JM, Srinivasan R (2012) Psychiatric drugs bind to classical targets within early exocytotic pathways: therapeutic effects. *Biol Psychiatry* 72:905–915.
- Lester HA, Lavis LD, Dougherty DA (2015) Ketamine inside neurons? *Am J Psychiatry* 172:1064–1066.
- Loryan I, Fridén M, Hammarlund-Udenaes M (2013) The brain slice method for studying drug distribution in the CNS. *Fluids Barriers CNS* 10:6.
- Mager S, Min C, Henry DJ, Chavkin C, Hoffman BJ, Davidson N, Lester HA (1994) Conducting states of a mammalian serotonin transporter. *Neuron* 12:845–859.
- Malhi GS, Mann JJ (2018) Depression. *Lancet* 392:2299–2312.
- Marvin JS, Borghuis BG, Tian L, Cichon J, Harnett MT, Akerboom J, Gordus A, Renninger SL, Chen TW, Bargmann CI, Orger MB, Schreiter ER, Demb JB, Gan WB, Hires SA, Looger LL (2013) An optimized fluorescent probe for visualizing glutamate neurotransmission. *Nat Methods* 10:162–170.
- Mateus A, Matsson P, Artursson P (2013) Rapid measurement of intracellular unbound drug concentrations. *Mol Pharm* 10:2467–2478.
- Mateus A, Matsson P, Artursson P (2014) A high-throughput cell-based method to predict the unbound drug fraction in the brain. *J Med Chem* 57:3005–3010.

- Mateus A, Treyer A, Wegler C, Karlgren M, Matsson P, Artursson P (2017) Intracellular drug bioavailability: a new predictor of system dependent drug disposition. *Sci Rep* 7:43047.
- Momo F, Fabris S, Stevanato R (2005) Interaction of fluoxetine with phosphatidylcholine liposomes. *Biophys Chem* 118:15–21.
- Muthusamy AK, Kim CH, Virgil SC, Knox HJ, Marvin JS, Nichols AL, Cohen BN, Dougherty DA, Looger LL, Lester HA (2022) Three mutations convert the selectivity of a protein sensor from nicotinic agonists to S-methadone for use in cells, organelles, and biofluids. *J Am Chem Soc* 144:8480–8486.
- Nguyen PT, Lai JY, Lee AT, Kaiser JT, Rees DC (2018) Noncanonical role for the binding protein in substrate uptake by the MetNI methionine ATP Binding Cassette (ABC) transporter. *Proc Natl Acad Sci U S A* 115: E10596–e10604.
- Nichols AL, Blumenfeld Z, Fan C, Luebbert L, Blom AEM, Cohen BN, Marvin JS, Borden PM, Kim C, Muthusamy AK, Shivange AV, Knox HJ, Campello HR, Wang JH, Dougherty DA, Looger LL, Gallagher T, Rees DC, Lester HA (2022) Fluorescence activation mechanism and imaging of drug permeation with new sensors for smoking-cessation ligands. *Elife* 11:e74648.
- Nierenberg AA, Farabaugh AH, Alpert JE, Gordon J, Worthington JJ, Rosenbaum JF, Fava M (2000) Timing of onset of antidepressant response with fluoxetine treatment. *Am J Psychiatry* 157:1423–1428.
- O'Brien FE, O'Connor RM, Clarke G, Dinan TG, Griffin BT, Cryan JF (2013) P-glycoprotein inhibition increases the brain distribution and antidepressant-like activity of escitalopram in rodents. *Neuropsychopharmacology* 38:2209–2219.
- Paulzen M, Lammertz SE, Gründer G, Veselinovic T, Hiemke C, Tauber SC (2016) Measuring citalopram in blood and cerebrospinal fluid: revealing a distribution pattern that differs from other antidepressants. *Int Clin Psychopharmacol* 31:119–126.
- Peters EJ, Reus V, Hamilton SP (2009) The ABCB1 transporter gene and antidepressant response. *F1000 Biol Rep* 1:23.
- Pfriefer FW, Ungerer N (2011) Cholesterol metabolism in neurons and astrocytes. *Prog Lipid Res* 50:357–371.
- Quan J, Tian J (2009) Circular polymerase extension cloning of complex gene libraries and pathways. *PLoS One* 4:e6441.
- Rao N (2007) The clinical pharmacokinetics of escitalopram. *Clin Pharmacokinet* 46:281–290.
- Renshaw PF, Guimaraes AR, Fava M, Rosenbaum JF, Pearlman JD, Flood JG, Puopolo PR, Clancy K, Gonzalez RG (1992) Accumulation of fluoxetine and norfluoxetine in human brain during therapeutic administration. *Am J Psychiatry* 149:1592–1594.
- Riad M, Watkins KC, Doucet E, Hamon M, Descarries L (2001) Agonist-induced internalization of serotonin-1a receptors in the dorsal raphe nucleus (autoreceptors) but not hippocampus (heteroreceptors). *J Neurosci* 21:8378–8386.
- Riad M, Zimmer L, Rbahl L, Watkins KC, Hamon M, Descarries L (2004) Acute treatment with the antidepressant fluoxetine internalizes 5-HT1A autoreceptors and reduces the *in vivo* binding of the PET radioligand [18F]MPPF in the nucleus raphe dorsalis of rat. *J Neurosci* 24:5420–5426.
- Salomon RM, Miller HL, Krystal JH, Heninger GR, Charney DS (1997) Lack of behavioral effects of monoamine depletion in healthy subjects. *Biol Psychiatry* 41:58–64.
- Schapiro MB, Attack JR, Hanin I, May C, Haxby JV, Rapoport SI (1990) Lumbar cerebrospinal fluid choline in healthy aging and in Down's syndrome. *Arch Neurol* 47:977–980.
- Scheepers GH, Lycklama ANJA, Poolman B (2016) An updated structural classification of substrate-binding proteins. *FEBS Lett* 590:4393–4401.
- Senese NB, Rasenick MM (2021) Antidepressants produce persistent  $\alpha_s$ -associated signaling changes in lipid rafts after drug withdrawal. *Mol Pharmacol* 100:66–81.
- Shivange AV, Borden PM, Muthusamy AK, Nichols AL, Bera K, Bao H, Bishara I, Jeon J, Mulcahy MJ, Cohen B, O'Riordan SL, Kim C, Dougherty DA, Chapman ER, Marvin JS, Looger LL, Lester HA (2019) Determining the pharmacokinetics of nicotinic drugs in the endoplasmic reticulum using biosensors. *J Gen Physiol* 151:738–757.
- Smith D, Allerton C, Kalgutkar A, van de Waterbeemd H, Walker D (2012) Pharmacokinetics and metabolism in drug design. Weinheim, Germany: Wiley.
- Søgaard B, Mengel H, Rao N, Larsen F (2005) The pharmacokinetics of escitalopram after oral and intravenous administration of single and multiple doses to healthy subjects. *J Clin Pharmacol* 45:1400–1406.
- Srinivasan R, Pantoja R, Moss FJ, Mackey EDW, Son C, Miwa J, Lester HA (2011) Nicotine up-regulates alpha4beta2 nicotinic receptors and ER exit sites via stoichiometry-dependent chaperoning. *J Gen Physiol* 137:59–79.
- Steinberg EM, Cardoso GM, Martinez PE, Rubinow DR, Schmidt PJ (2012) Rapid response to fluoxetine in women with premenstrual dysphoric disorder. *Depress Anxiety* 29:531–540.
- Tavoulari S, Forrest LR, Rudnick G (2009) Fluoxetine (Prozac) binding to serotonin transporter is modulated by chloride and conformational changes. *J Neurosci* 29:9635–9643.
- Tischbirek CH, Wenzel EM, Zheng F, Huth T, Amato D, Trapp S, Denker A, Welzel O, Lueke K, Svetlitchny A, Rauh M, Deusser J, Schwab A, Rizzoli SO, Henkel AW, Müller CP, Alzheimer C, Kornhuber J, Groemer TW (2012) Use-dependent inhibition of synaptic transmission by the secretion of intravesicularly accumulated antipsychotic drugs. *Neuron* 74:830–844.
- Trapp S, Rosania GR, Horobin RW, Kornhuber J (2008) Quantitative modeling of selective lysosomal targeting for drug design. *Eur Biophys J* 37:1317–1328.
- Treyer A, Mateus A, Wiśniewski JR, Boriss H, Matsson P, Artursson P (2018) Intracellular drug bioavailability: effect of neutral lipids and phospholipids. *Mol Pharm* 15:2224–2233.
- Treyer A, Walday S, Boriss H, Matsson P, Artursson P (2019) A cell-free approach based on phospholipid characterization for determination of the cell specific unbound drug fraction ( $f_{u,cell}$ ). *Pharm Res* 36:178.
- Tucker KR, Block ER, Levitan ES (2015) Action potentials and amphetamine release antipsychotic drug from dopamine neuron synaptic VMAT vesicles. *Proc Natl Acad Sci U S A* 112:E4485–E4494.
- Unger EK, et al. (2020) Directed evolution of a selective and sensitive serotonin sensor via machine learning. *Cell* 183:1986–2002.e26.
- Vargas HM, Jenden DJ (1996) Elevation of cerebrospinal fluid choline levels by nicotinamide involves the enzymatic formation of N1-methylnicotinamide in brain tissue. *Life Sci* 58:1995–2002.
- Wan H, Rehgren M, Giordanetto F, Bergström F, Tunek A (2007) High-throughput screening of drug-brain tissue binding and *in silico* prediction for assessment of central nervous system drug delivery. *J Med Chem* 50:4606–4615.
- Wong DT, Horng JS, Bymaster FP, Hauser KL, Molloy BB (1974) A selective inhibitor of serotonin uptake: lilly 110140, 3-(p-trifluoromethylphenoxy)-N-methyl-3-phenylpropylamine. *Life Sci* 15:471–479.
- Wong DT, Bymaster FP, Engleman EA (1995) Prozac (fluoxetine, Lilly 110140), the first selective serotonin uptake inhibitor and an antidepressant drug: twenty years since its first publication. *Life Sci* 57:411–441.
- Wong DT, Perry KW, Bymaster FP (2005) Case history: the discovery of fluoxetine hydrochloride (Prozac). *Nat Rev Drug Discov* 4:764–774.
- Yu H, Dickson EJ, Jung SR, Koh DS, Hille B (2016) High membrane permeability for melatonin. *J Gen Physiol* 147:63–76.
- Zeisel SH, Epstein MF, Wurtman RJ (1980) Elevated choline concentration in neonatal plasma. *Life Sci* 26:1827–1831.